Title

Understanding the Formation-Structure-Functionality Relationship of the Catalyst Layer in a Proton Exchange Membrane Fuel Cell

Permalink

https://escholarship.org/uc/item/86x496m7

Author

Yang, Donglei

Publication Date

2021

Supplemental Material

https://escholarship.org/uc/item/86x496m7#supplemental

Copyright Information

Peer reviewed|Thesis/dissertation

UNIVERSITY OF CALIFORNIA, MERCED

Understanding the Formation-Structure-Functionality Relationship of the Catalyst Layer in a Proton Exchange Membrane Fuel Cell

A Dissertation submitted in partial satisfaction of the requirements
for the degree of Doctor of Philosophy

in

Mechanical Engineering

by

Donglei Yang

Committee in charge:
Professor Po-Ya Abel Chuang, Chair
Professor Min Hwan Lee
Professor Ashlie Martini
Professor Venkattraman Ayyaswamy

2021

The Dissertation of Donglei Yang is approved, and it is acceptable in quality and form for publication on microfilm and electronically:

Prof. Po-YaAbel Chuang, Chair	Date

Prof. Min Hwan Lee	Date

Prof. Ashlie Martini	Date

Prof. Venkattraman Ayyaswamy	Date

University of California, Merced

2021

Dedicated to the universe and nature.

Table of Contents

List of Figures

List of Tables

Acknowledgement

It is surprising to realize my journey of PhD has come to an end. When I joined the PhD program, my purpose was to do quality research and to become an independent researcher by graduation. During these past few years, I have been inspired so much by our excellent and friendly faculty on campus, not only because of their research but more importantly because of themselves as experienced researchers.

First and foremost, I would like to thank my advisor, Prof. Abel Chuang, for his enduring support on this research and warmhearted advices on life.

I would like to sincerely thank both current and former committee members, Prof. Min Hwan Lee, Prof. Ashlie Martini, Prof. Venkattraman Ayyaswamy, Prof. Arvind Gopinath, and Prof. Anand Subramaniam not only for their support and truthful feedback on this research, but also for their kindness and willingness to share their research experience and wisdom.

I would also like to thank Prof. Christopher Viney and Prof. Christin Isborn for the early discussion, Prof. Andy LiWang for his kind support, Mike Dunlap for hid training and aid on imaging, Dr. David Rice for his patient training and aid on NMR measurements.

Thank Felipe Mojica, Maricor Divinagracia, Jose Flores, and Mrittunjoy Sarker for their contribution to this work.

Additionally, I would like to thank Distinguished Professor Emeritus Michael Modest, Dr. Robert Rice, Dr. Huifang Dou, Prof. Yue (Jessica) Wang, Prof. Jennifer Lu, Prof. Fabian Filipp, Prof. Michael Scheibner, Prof. Gerardo Diaz, and Prof. Jian-Qian Sun for their kind suggestions on professional and personal growth.

Thank my dear family, friends, and lab mates for their company and support along my journey.

Curriculum Vita

Education

Doctor of Philosophy, Mechanical Engineering, University of California, Merced   05/2021

Master of Engineering, Chemical Engineering, University of Chinese Academy of Sciences, China   07/2014

Bachelor of Engineering, Chemical Engineering and Technology (em. Electrochemistry), Harbin Engineering University, China   07/2010

Selected publications

D. Yang; M. Divinagracia; F. Mojica; J.D. Ocon; P. A. Chuang. The origin of heterogeneity of hierarchical catalyst layer microstructure. 2021. J. Electrochemical Society. In review.

D. Yang; F. Mojica; M. Sarker; P. A. Chuang. The structure-functionality relationship of catalyst layer. 2021. J. Electrochemical Society. In review.

D. Yang, P. A. Chuang. Perspective on the design of catalyst layers. In preparation.

D. Yang, P. A. Chuang. An ultrathin electrode for hydrogen polymeric electrolyte fuel cells. Patent. In preparation.

D. Yang; P. A. Chuang. Precise control of structure-functionality relationship of catalyst layers. In preparation.

D. Yang, P. A. Chuang. Rheological study of electrode ink for a PEMFC: I/C and solid content. 235th Electrochemistry Society Meeting, Dallas, 2019, May 26-30.

D. Yang, P. A. Chuang. Probing electrode microstructure by ink rheology. Gordon Research Conference on Fuel Cells, Boston, 2018, Jul. 29 – Aug. 3.

G. Li and D. Yang; P. A. Chuang. Defining Nafion ionomer roles for enhancing alkaline oxygen evolution electrocatalysis, ACS Catalysis, 2018, 8(12), 11688-11698.

D. Yang, P. A. Chuang. Study of electrode ink rheology and coating quality for PEM fuel cell application. APS Annual Meeting, Merced, 2017, Nov. 2-4.

H.-M. Yu; D. Yang; Y. Zhao; Y. Liu; Z. Shao. The preparation of alkaline anion exchange membrane fuel cell MEA, 2016, Patent No.: CN201310086097.8, granted.

D. Yang; H. Yu; G. Li; Y. Zhao; Y. Liu; C. Zhang; W. Song; Z. Shao. Fine microstructure of high-performance electrode in alkaline anion exchange membrane fuel cells, J. Power Source, 2014, 267: 39-47.

D. Yang; H. Yu; G. Li; W. Song; Y. Liu; Z. Shao. Effect of gas diffusion electrode parameters on anion exchange membrane fuel cell performance, Chin. J. Catalysis, 2014, 35: 1091-7.

Field of study

Complex fluids, composite thin films, electrochemical devices.

Donglei Yang
Mechanical Engineering
University of California, Merced, 2021
Chair Professor Po-Ya Abel Chuang

Understanding the Formation-Structure-Functionality Relationship of the Catalyst Layer in a Proton Exchange Membrane Fuel Cell

ABSTRACT

Proton exchange membrane fuel cell (PEMFC) technology provides a sustainable power solution as it electrochemically converts the chemical energy stored in hydrogen molecules into electricity, heat, and water. The electrochemical reactions occurring in the catalyst layer (CL), however, requires the use of precious group metal (PGM) catalysts, such as platinum, which is a major factor contributing to the high cost of PEMFC technology. To reduce the cost, there have been extensive research efforts in developing low-PGM and PGM-free catalyst materials. Nevertheless, the CLs incorporating these novel materials are often found to suffer from severe mass transport resistance resulting in significant performance loss. Based on the literature, this undesired mass transport resistance is mainly attributed to the cathode oxygen transport due to the heterogeneous characteristics of the hierarchical microstructure of the CL. Although a standard CL only contains carbon supported catalyst and ionomer, understanding the formation of the structure and the origin of the structural characteristics have been very challenging due to its complicated preparation process. A CL is usually prepared by an ink casting method, which involves multiple steps. The catalyst ink consists of the CL constituent materials uniformly dispersed in a liquid medium forming a suspension, which has an opaque, heterogeneous, and highly time-sensitive nature making the experimental investigation on the particulate structure in the catalyst ink very challenging. Despite the long history of using the CLs, a principled framework for understanding the structure-property relationship of the CLs has not yet fully developed. To advance the design and development of low-cost and robust CLs, this research 1) conceptualized a physical process capturing the key aspects of the particulate structure formation with respect to the CL fabrication process, 2) based on the complex fluid nature of the catalyst ink, designed a holistic non-destructive hierarchical approach to investigate the particulate structure in the catalyst ink, and 3) qualitatively and experimentally established the formation-structure-process-functionality relationship for CLs. With the newly proposed framework, this research advances current understanding on the structure-property relationship of the CLs and provides novel and practical insights into the design of low-cost functionality-tailored CLs.

CHAPTER 1

INTRODUCTION

A quarter of human energy consumption is used for transportation and the total energy demand is expected to grow by more than 25% to 2040.[1-3] Hydrogen fuel cells generating only electricity, water and heat provide a promising solution to the sustainability of modern society. With the advantages of fast refueling, low operating temperature and quick response to load change, proton exchange membrane fuel cells (PEMFCs) has great potentials in applications for transportation.[4-6]

1.1 PEMFCs

A PEMFC is an electrochemical power device. It generates electricity by converting chemical energy stored in hydrogen through electrochemical reactions while rejecting only heat and water. Unlike batteries which stores energy within the electrode materials, PEMFCs produce electricity as long as hydrogen is supplied. The working principle of a PEMFC can be expressed as:

$$\text{Overall: } H_2 + \frac{1}{2}O_2 = H_2O \tag{1.1}$$

$$\text{Anode: } H_2 = 2H^+ + 2e^- \tag{1.2}$$

$$\text{Cathode: } \frac{1}{2}O_2 + 2H^+ + 2e^- = H_2O \tag{1.3}$$
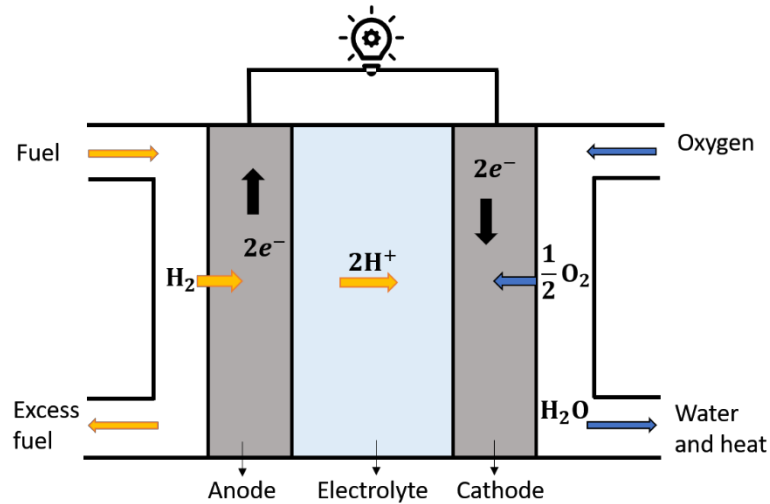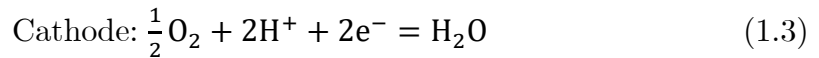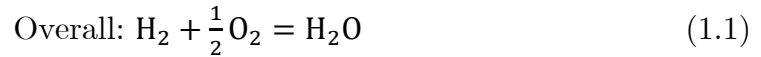
Figure 1.1. A schematic drawing of a PEMFC.

A simple schematic diagram of a PEMFC is provided in Figure 1.1. With the help of electrocatalyst (such as platinum), the overall reaction (Eq. 1.1) is split into two electrochemical reactions occurring at the two electrodes of a PEMFC, anode and cathode, respectively. At the anode, hydrogen molecules are oxidized by anodic catalyst to produce protons and electrons (Eq. 1.2). The negatively charged electrons travel to the cathode through external circuit generating electricity. Meanwhile, the positively charged protons are transferred through internal electrolyte (proton exchange membrane, PEM) towards the cathodic side. Finally, these electrons and protons meet up at the catalyzed cathode allowing oxygen reduction reaction to occur producing water and heat (Eq. 1.3).

The combination of anode, PEM and cathode consists of the key component of a PEMFC, membrane electrode assembly (MEA). MEA is the heart of PEMFC as it is where electrode reactions take place. In practice, an MEA is a lamination of PEM sandwiched by anodic and cathodic catalyst layers, and anodic and cathodic gas diffusion media (Figure 1.2). The PEM separates the reactant gases and serves as a proton carrier. The catalyst layers containing electrocatalyst provide reaction sites and transport channels for reaction species, i.e. protons, electrons, reactant gases and water. The gas diffusion media outside of catalyst layers are responsible for both transport of reactants into catalyst layers and removal of generated water. Within an MEA, catalyst layers are the major components responsible for performance, durability, and cost.
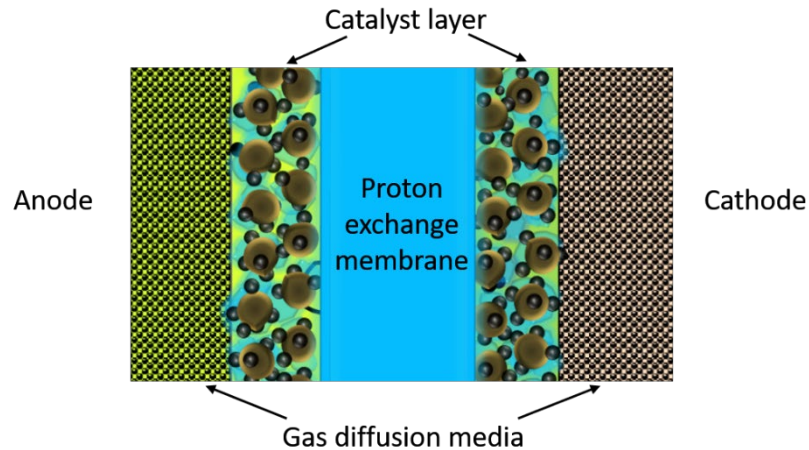
Figure 1.2. A schematic drawing of a membrane electrode assembly (MEA).

Recent small-scale commercial application of PEMFCs in electric vehicles has demonstrated their potential success in large-scale transportation application.[6] However, the system cost still hampers PEMFC technology being widely acceptable, even though it has dropped 67% in the past few years.[7] One of the major

2

components of the PEMFC system cost is the electrode cost. Currently, both the cathode and anode require platinum-group metals (PGMs) to catalyze the electrode reactions. Owing to sluggish oxygen reduction reaction at the cathode (about 5 orders of magnitude slower than anode reaction), the majority of PGMs are required at the cathode.[8] As PGMs are commodities and scarce, increased demand for PEMFC will require reduced or eliminated PGM loading to lower the catalyst cost. It is predicted that even at large manufacturing volume catalyst cost due to high PGM loading remains the most significant barrier for further cost reduction.[6-7, 9] To achieve further cost reduction without compromising cell performance, understanding, and developing electrodes with reduced or no use of PGM catalyst have become the first priority.[9-11]

1.2 Catalyst layers

Catalyst layers (CLs) have been extensively used as the PEMFC electrodes since the invention in 1990s.[12-13] In the structure of this conventional CL, the impregnation of proton-conductive ionomer and the use of carbon-supported catalyst significantly enhance the contact at membrane|CL interface and inside the CL the contact at ionomer|catalyst interfaces. Consequently, the reaction sites within the CL are maximized leading to high utilization of the catalyst and reduced catalyst loading.

Due to the ease of fabrication and scalability, to date this state-of-the-art structure of CL is still widely used.[10, 14-18] To optimize the triple phase interface and reduce the use of PGM catalyst, other types of CLs have been developed as well, e.g. nanofiber-based CLs,[19-20] nanostructured CLs.[21-22] The scope of this research will focus on conventional CLs.
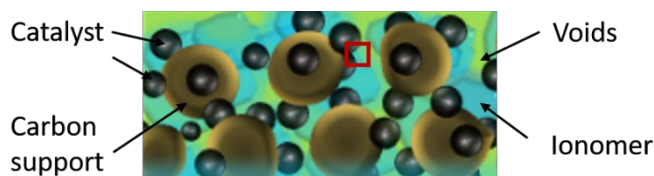
Figure 1.3. A schematic drawing of catalyst layer. The red square represents one of the triple phase interfaces.

Cost reduction in electrode with improved performance and durability is the key to make PEMFC widely acceptable. Precise control of electrode microstructure for optimal performance and maximum material utilization is the ultimate goal of electrode design. This is because electrode microstructure not only governs the utilization of electrode constituent materials, but also determines the transport property at high current density.

As mentioned earlier, electrode reactions take place within the CLs. Inside a CL triple phase interfaces (represented by the red square in Figure 1.3), where gas, ionomer and catalyst coexist, are responsible for providing effective reaction sites.[23-24] Only with continuous accesses to gaseous, protonic, and electronic pathways, these reaction sites contribute to the electrochemical reactions. The efficiency of various pathways is influenced by the logistics of through pore, ionomer distribution and connectivity of catalyst/support particles. Hence, the microstructure of a CL affects its electrochemical performance.

Recent research on low-PGM CLs have shown that these low-loading CLs suffer from voltage loss at high current density.[25-27] The main cause of the voltage loss has been found to be diffusion-type mass transport, which originates from the microstructure of CL regarding catalyst-ionomer agglomerate, roughness factor, pore property for water management.[25, 27-31] As for PGM-free CLs, due to low mass activity of PGM-free catalyst comparing to PGM catalyst, the CLs are often 20 times thicker accompanied with sever mass transport issue at high current density. By tuning proton conductivity, porosity and water management in the electrode, optimal performance of PGM-free CLs can be achieved.[14, 32-33] However, the current challenge is how to properly integrate PGM-free catalysts with synergistic CL design. To advance the design of next-gen CLs, developing fundamental knowledge for precise control of CL microstructure is necessary.[10-11, 16, 34-38]

1.3 Membrane electrode assembly design and fabrication

Figure 1.4 shows a typical MEA fabrication process. A CL prepared from a catalyst ink—a colloidal dispersion consisting of catalyst/support nanoparticles (e.g. Pt/C with Pt dia. 2-5 nm and carbon dia. 30-70 nm[39]), ionomer (weight-average molar mass 2.5×10^5 g/mol [40]) and dispersing medium—is coated on a substrate and dried forehand. Two pieces of the CLs (anode and cathode) are transferred onto each side of a PEM via decal transfer method to form a catalyst-layer-coated-membrane (CCM) electrode. Sandwiched by two pieces of gas diffusion medium, this CCM electrode is then hot pressed becoming an MEA, which finally can be used in a PEMFC to generate electricity.
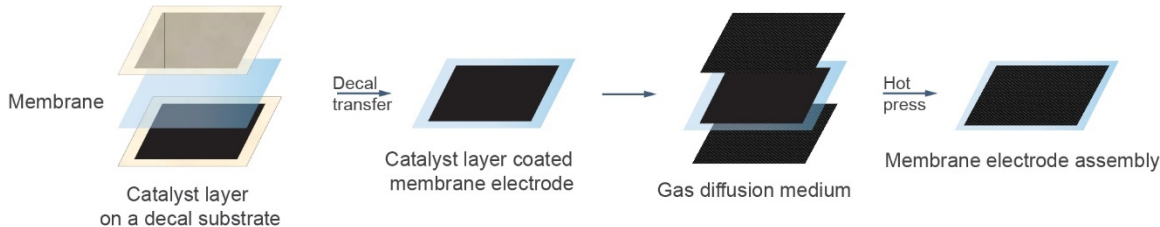
Figure 1.4. A typical process of MEA fabrication.

As discussed in section 1.2, the microstructure of the thin film CL plays a critical role in regulating the material utilization and transport property of PEMFC electrode. Despite the choice of the materials, enormous evidence has shown that the ink formulation and coating method also have a strong impact on the resulting electrode microstructure and performance.[17, 41-43] This is because regardless of the employed coating methods such as roll-to-roll,[44-46] slot-die,[47] screen printing,[48-49] and spraying,[50-53] practically the microstructure of CL takes the shape from the catalyst ink and deforms through coating processing then solidifies into the final structure. In other words, the microstructure of the CL is an accumulated consequence of both catalyst ink formulation and the application processes. Therefore, to facilitate the design of next-gen CL, understanding the microstructure formation of CL from the catalyst ink through the coating process is critical.

CHAPTER 2

LITERATURE REVIEW

The microstructure of CL is a consequence of both CL materials and processing as inputs. The output is the electrochemical and transport properties. To facilitate the design of next-gen CL, understanding the microstructure formation of CL from the catalyst ink with respect to the coating process is critical. It requires knowledge of underlying physics and phenomena from multicomponent dispersions and catalyst inks, to coating or processing, and then to the final microstructure of CL.[54-56]

2.1 Catalyst inks

The structure of the state-of-the-art CL is formed by casting catalyst inks.[12, 43, 49, 57] Three major components comprise the catalyst ink, i.e. supported catalyst particles, polyelectrolyte ionomer, and dispersing medium. Standard ingredients are Pt/C, perfluorosulfonic acid (PFSA) ionomer, water-alcohol mixture.

Extensive empirical evidence have shown that optimal structure and performance of CLs can be achieved by adjusting the formulation of catalyst inks, which indicates the significance of interplay between these ink components.[51, 58-65]. The liquid|solid interaction governs the interfacial energy of the solid particles and thus affects the size distribution of aggregates and agglomerates. The liquid|ionomer interaction determines the conformation of ionomer and thus the size of ionomer aggregates and their behavior at liquid|solid interfaces. The behavior of ionomer aggregates at liquid|solid interfaces determines the colloidal structure of agglomerates of ionomer and solid particles, which in turn affects the formation of triple phase interface. In the CL, the optimal electrochemical performance is a result of well-percolated microstructure with precise and uniform ionomer distribution. Therefore, many efforts have been put into understand the ionomer conformation and adsorption behavior at the catalyst/support interfaces in various dispersing media.

Depends on the dispersing media, PFSA ionomer exhibits different colloidal morphology and gelation behavior.[66-67] In most aprotic dispersing media (e.g. dimethylacetamide and N-methylformamide), ionomer exhibits a random-coil conformation (true solution behavior) and undergoes homogeneous, thermally

reversible gelation behavior. In pure alcoholic dispersing media (e.g. methanol, ethylene glycerol, glycerol), ionomer shows a well-defined cylindrical conformation with different degrees of solvation and undergoes inhomogeneous, thermally irreversible gelation as films. In water/monohydric alcohol mixtures (e.g. water/methanol, water/ethanol, water/IPA), ionomer exists as a less-defined, highly solvated large particle and undergoes inhomogeneous, thermally irreversible gelation with the formation of an ordered lamellar-type in the sol phase and precipitates in the gel phase.

In aqueous environment, Nafion ionomer adsorption on the surface of catalyst/support particle was found to have a saturation concentration.[68-69] A primary adsorption following Langmuir isotherm seems to occur at the outer surface of the particle till adsorption saturation, which is then followed by a secondary adsorption. Ionomer interaction with catalyst/support particle was also found to be stronger than the interaction with support particles alone, suggesting a preferred adsorption at the catalyst surface. While in an isopropyl alcohol aqueous environment, interaction between ionomer and bare support surface was found to be dominated by van der Waals attraction force.[70] Molecular dynamic simulation also predicts that in the water-rich environment, ionomer is highly aggregated with hydrophilic side chain at the outer surface of the aggregates surrounding the hydrophobic backbone domain.[71] Adsorption of ionomer on the support surface is predominantly via the backbone with side chains pointing away from the support surface. Addition of alcohol enhances ionomer dissolution leading to desorption from the support surface.

2.2 The particulate structure

There exist extensive studies regarding ink composition materials. However, due to highly dynamic, opaque and heterogenous nature of catalyst ink, obtaining experimental data of detailed structure of catalyst ink are challenging. The significance of the heterogenous structure of catalyst inks as a whole was rarely recognized until recent rising desire of understanding the nano- and microstructure for designing low-loading and PGM-free CLs.[16, 37-38, 55-56, 72]

Both computational and experimental results have shown that within the catalyst ink, ionomer aggregates, catalyst/support aggregates and colloidal agglomerates of ionomer and catalyst/support coexist.[37, 39, 73-74] Characterized by ultra-small-angle X-ray scattering and cryogenic transmission electron microscopy, it was found that the structure of catalyst inks is heterogeneous at multilevel [39]. Ink particles were found to consist of rod-like ionomer aggregates 3 nm in diameter and 20 nm in length, spherical carbon 50-80 nm in diameter, rod-like carbon aggregates 150-350 nm in diameter and agglomerates of carbon aggregates > 400

nm in length. Size of Pt/C and ionomer also change with ink composition. Results of contrast-variation small-angle neutron scattering using inks with various concentration revealed that the major structural components of aqueous catalyst ink are colloids of supported-catalyst nanoparticles as the core (radius ~ 42 nm) and weakly adsorbed ionomer as outer shell (radius > 50 nm).[54, 74] Freeze-dried microstructure of a "real" catalyst ink visualized by cryogenic scanning electron microscopy also shows agglomerates of catalyst/support nanoparticles surrounded by spiderweb-like ionomer network.[17] The size of these agglomerates has a bimodal nature with one peak ~200 nm and another > 1μm. The study also shows that the heterogeneity of the ink microstructure varies with dispersing medium composition. Further study by cryogenic transmission electron microscopy reveals that within catalyst ink rod-like ionomer aggregates are strongly attracted to the surface of Pt rather than carbon support leaving a higher ionomer density than the bulk area.[35] This result indicates ionomer network observed in the freeze-dried ink structure as a result of distortion due to material contraction during freeze drying.

Experimental investigation on formation mechanism of CL microstructure is challenging. The ink agglomerate formation in CLs based on colloidal dispersion in an alcoholic environment was firstly simulated by coarse-grained molecular dynamics.[73] Phase segregation between ionomer phase and catalyst/support aggregates was observed. Catalyst/support particles aggregate rapidly with a randomly interconnected proton-conducting network is formed by ionomer domains whose backbones are attached to the surface of carbon agglomerates while side chains are buried in hydrophilic domains away from vicinity of the particles. The interior of the agglomerate is ionomer free. The resulting microstructure of CL depends on carbon size distribution and ionomer-carbon interaction which is affected by the polarity of the dispersing medium. As for the formation of pore structure in the CL, a hypothetical mechanism based on both experiment results and theoretical model suggests that pores in the CL originate from the movement of colloidal agglomerates of ionomer coated catalyst/support in the catalyst ink throughout the application process.[37] Agglomeration of ionomer-catalyst/support colloids induces the formation of heterogeneous pores and affects ionomer distribution in the CL.

2.3 Application processes
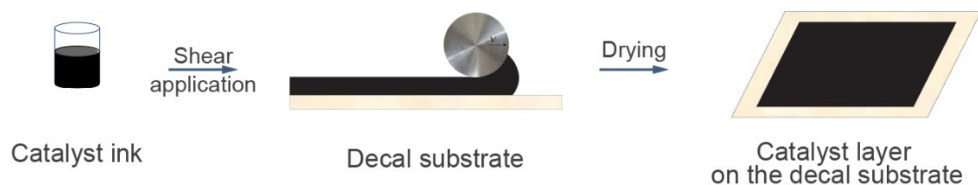
Figure 2.1. A typical ink application process for catalyst layer fabrication.

To elucidate the formation of catalyst microstructure, it is necessary to understand the physics that the ink microstructure experiences throughout the fabrication process. Figure 2.1 illustrates a simplified process to fabricate CLs from catalyst inks. From catalyst ink to CL, the ink colloids undergo shear deformation and solidification to form the final 3D fractal particle networks.

In the literature, solidification has been long considered as the only factor affecting formation of pristine microstructure of CLs.[17, 37, 73, 75-76] At nanoscale, it was found by contrast-variation small-angle neutron scattering that during ink evolution or solidification shrinkage of ink agglomerates occurs.[75] Size of the solid core of catalyst/support aggregates, size of nanopores between primary catalyst/support particles and the thickness of the ionomer corona all decrease, accompanied with the formation of ionic channels in the polymer matrix. At microscale, visualization of catalyst inks by atmospheric in-situ SEM shows two steps of structure solidification, sedimentation and shrinking.[76] During shrinking, particle migration phenomena was observed, which is considered the mechanism of non-uniform particle distribution.[37, 77]

2.4 The formation of the particulate structure

Investigation on CL structure formation process through experimental approach has been rather challenging, since the heterogeneous CL structure is usually formed from a liquid suspension of the CL constituent materials, i.e. a catalyst ink, which has a dynamic, opaque, and heterogenous nature.[56] To our best knowledge, only a handful of direct studies have attempted, mainly through computational approaches. The structural evolution process of a simplified carbonaceous ink system, from randomly distributed materials in the suspension to the phase-segregated agglomerates of ionomer clusters and carbon aggregates in the CL, depending on the liquid media, was firstly revealed using a coarse-grained molecular dynamic model (CGMD).[73] The self-assembling of the analogous carbon system was observed without considering the effect from the presence of the PGM catalyst. After including Pt in an extended CGMD model, the local ionomer morphology and thin film distribution on the Pt/C surfaces were found distinct from those on the mere carbon surfaces, due to the ionomer structural dependence on the wettability of Pt/C surface.[78] Also using a carbonaceous system, the

formation process of large pores and large agglomerates present in the CL structure was unraveled via an agglomerate model combined with colloidal Derjaguin-Landau-Verwey-Overbeek theory and a dynamic particle packing model based on discrete element method and multisphere method.[37, 79] The CL heterogeneous structure and the oxygen diffusion in the CL were found affected by the adhesion and migration of the ionomer cluster and the packing of the carbon aggregates. These insights provide a glimpse of the complexities of the CL structure formation process.

Over a decade, progress of experimental investigation has been gradually made with the aid of various scattering and spectroscopic tools, but mainly on the microstructure of the catalyst inks. Earlier, the hierarchical structure of the particles inside the catalyst inks, including primary particles, aggregates of primary particles, and agglomerates of aggregates, depending on the liquid media, was first time revealed using ultra-small-angle X-ray scattering and cryogenic transmission electron microscopy.[39] The catalyst inks were found to be heterogeneous, containing non-uniformly distributed small (dia. < 70 nm) particles of individual components (i.e. Pt/C and ionomer) and large (dia. > 300 nm) Pt/C aggregates and ionomer-Pt/C agglomerates, and differ from those of the individual component dispersions. The size and the structure of the Pt/C agglomerates and ionomer particles were also found to change significantly with different liquid environment employed. Further, more details on the structure of the catalyst inks were discovered using focusing- and contrast-variation small-angle neutron scattering in the dilute systems with water as the liquid media.[74-75] The catalyst inks were found containing phase-segregated ionomer-Pt/C agglomerates, where the Pt/C phase has a percolating cluster structure and mediated by the ionomer phase, which contains ionic clusters in the liquid phase. More recently, the particulate structures inside the catalyst inks, with water/1-propyl alcohol (NPA) binary liquid systems, were first time visualized using cryogenic scanning electron microscopy.[17] The heterogeneous structural characteristics commonly observed in the CL, such as inhomogeneous ionomer distribution and randomly distributed varisized ionomer-Pt/C agglomerates, depending on the water/NPA weight ratios, were also observed in the catalyst inks. Relatively large strongly segregated ionomer-Pt/C agglomerates and high-density small well-coated ionomer-Pt/C agglomerates were observed with bimodal size distributions in the water-rich and NPA-rich catalyst inks, respectively. The structures of the heterogeneous agglomerates were also found to be changeable depending on the water/NPA weight ratios, signifying the complex role of the liquid environment on the formation of the ionomer-Pt/C agglomerate structure. Although much progress has been made in understanding

the structure of the catalyst inks, systematic experimental investigations on the structure translation from catalyst inks into CLs are still lacking.[55]

To realize precise control of the CL structure with tailored transport properties, a proper frame of knowledge on the CL structural formation process is required and needs to be developed. As mentioned earlier, the CL is often made from a catalyst ink, a liquid suspension comprising carbon-supported catalyst nanoparticles, ionomer, and the liquid medium. As shown in Figure 2.2, with the materials of choice, the CL fabrication process mainly includes but is not limited to the preparation of the catalyst ink, the deposition of the ink, and the removal of the liquid medium. The preparation is usually done by ultrasonication, magnetic stirring, and ball milling etc., which produce various extents of shear force through the liquid phase to break up and mix the aggregates in the materials.[80-82] The deposition methods are commonly roll-to-roll,[44-46] slot-die,[47] screen printing,[48-49] spraying,[50-53] inkjet printing, and brushing, to name a few. These methods spread the catalyst ink suspension into a thin wet film at certain speed, generating a shear gradient throughout the thickness of the deposited wet film, which solidifies a pristine CL. The liquid removal can be done by many drying methods, which have been summarized and investigated in the reference.[83] Despite the current knowledge on the microstructure of the catalyst inks, the role of shear involved in the CL fabrication process remains overlooked.
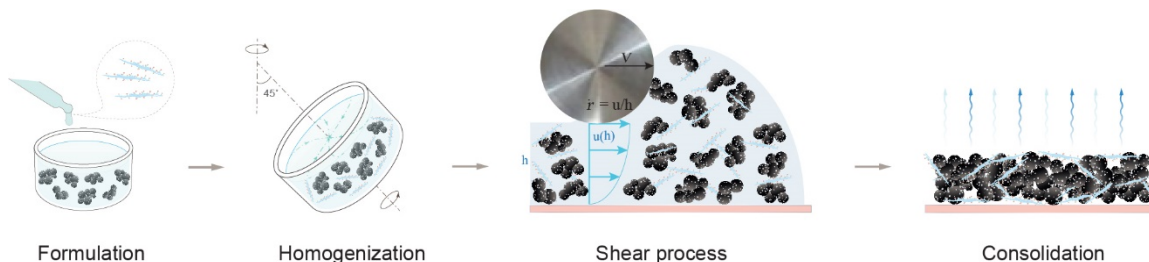
Figure 2.2. Schematic diagram of the physics behind catalyst layer fabrication process. (Drawings are not to scale.)

In fact, the CL formation process is quite similar to a sol-gel-derived film formation process, which includes the preparation of a sol, film deposition prior to the gelation of the sol, and the removal of the liquid medium.[84] In the sol-gel system, a sol is a liquid suspension of solid particles, whose size can broadly range from one to 1000 nm as long as no severe particle sedimentation due to gravity.[85-86] A gel is a coherent mass comprising a continuous rigid skeleton phase and a continuous liquid phase.[87] The solid particles in the sol can grow into the percolating skeleton

in the gel through various aggregation mechanisms, forming linking clusters till a single space-filling cluster (i.e. the gel point) and beyond, with isolated clusters around. Analogous to the sol-gel system, the structure formation process of the CLs likely include: 1) dispersion and assembly of constituent nanomaterials,[73] 2) formation of fractal aggregates,[39] 3) clustering of impinging aggregates,[88] 4) gelation of linking clusters,[88-89] 5) evolution and deformation of the network alongside/after gelation,[74-75, 90] and finally 6) structural consolidation due to liquid evaporation.[84-85] Notably, precise structure of the sol-gel-derived film can be achieved based on the underlying physics and chemistry of sol-gel film formation, by controlling the sol structure, such as particle size and fractal property, and by controlling the gel structural evolution induced by shear and other factors during film formation.[84] Such a feature of the sol-gel derived films is rather important, because it means that CLs with functionality-tailored micro- and nanostructure can be achieved by precisely control not only the ink microstructure but also the nanostructure and the translation of this multiscale structure into the CL.

Different from the sol-gel-derived film, the CL contains ionomer, which is critical to both the function and the structure of the CL. On one side, the ionomer is the electrolyte, the spatial distribution of which governs the ionic transport. On another, as mentioned earlier, the ionomer causes undesired structural heterogeneity that hampers the oxygen transport and diminishes the PGM material utilization. Thus, to achieve precisely controlled structure-property relationship for the CLs, the CL structure formation process regarding the interfacial and spatial distribution of the ionomer phase needs to be understood in particular. PFSA is the most commonly used CL ionomer. Its molecular structure consists of a hydrophobic perfluorocarbon main chain and hydrophilic sulfonated vinylether side chains.[91] Due to the incompatibility between the main chain and the side chain, the morphology of the PFSA ionomer in a liquid medium is highly affected by the liquid composition, such as the water/alcohol ratio of a water-alcohol binary solvent.[42, 66-67, 92] Moreover, the morphology of the ionomer in the liquid medium has been found to relate to the local morphology of ionomer nanofilm on the catalyst surface.[93] If considering the ionomer as a surfactant, the ionomer in the liquid phase may diffuse, attach, and rearrange to be adsorbed onto PGM/C surfaces during the preparation of a catalyst ink.[94] Alternatively, depending on the liquid medium, the ionomer conformation and the interaction between the ionomer and the PGM/C surfaces can greatly affect the interfacial and spatial distribution of the ionomer,[73, 78, 95] the structure and dynamic behavior of the ionomer-PGM/C agglomerates,[18, 39, 70, 72] and the structure-property relationship of the resulting CL.[25, 96-97] Yet, systematic understanding on the hierarchical formation process of the CL structure is still missing.

2.5 Mass transport resistance and the particulate structure

The transport resistance present in the low-PGM and PGM-free CLs undesirably deteriorate the fuel cell performance at high current density and durability.[7, 98-99] This resistance has been shown to predominantly associate with oxygen transport in the heterogeneous structure of the cathode CL.[27, 100-103]

From the perspective of physics, inside the cathodic CL of an operating fuel cell, oxygen molecules migrate to the reaction sites through multiple phases, including pores, ionomer thin films, and liquid water if any. In the pores, oxygen molecules diffuse through different mechanisms with dependency on the pore size. When the pore size is larger than the oxygen molecule mean free path, transport or Fickian diffusion, i.e. the molecule-molecule collisions, dominates; when the pore size is comparable to and smaller than the oxygen molecule mean free path, Knudsen diffusion, i.e. the molecule-solid collisions, dominates. In the Knudsen regime, geometrical details of the pore structure has been proved to greatly affect the gas self-diffusion.[104-105] As for the ionomer phase, oxygen molecules firstly need to be adsorbed and dissolved at the void|ionomer interface, then diffuse through ionomer phase and finally reach the catalyst surface to be adsorbed on the reaction sites.[34, 37, 106] By manipulating the local morphology of the ionomer thin film, oxygen transport can be improved significantly.[97, 107] When liquid water presents, the oxygen transport becomes complicated as water can provide shortcut in the ionomer phase but also blocks pores at the same time.[27, 36, 102] Since the pore structure and the ionomer spatial distribution are governed by the microstructure of the CL, the oxygen transport can be affected by the microstructural details of the CLs.

From the perspective of CL structure, the hierarchical heterogeneities, such as inhomogeneous ionomer coverage and varisized agglomerates, greatly affect the effectiveness of both the reaction sites and the transport pathways for not only oxygen molecules but also protons.[10, 97, 108] Regarding oxygen transport, especially at nanoscale, the anisotropic morphology of ionomer thin film (4-20 nm thick) adjacent to PGM nanoparticles hinders the local oxygen transport. The domain-connectivity and hydrophobic matrix of PFSA ionomer competingly affect the dissolution and diffusion of oxygen through ionomer thin film.[91] In particular, the hydrophobic crystallite matrixes (approximately 2 nm) hamper the oxygen diffusing through ionomer thin film, resulting in nearly zero oxygen concentration at PGM catalyst surface.[106, 109] At mesoscale, the spatially non-uniform thickness and inhomogeneous distribution of ionomer presenting in both the percolating network and the agglomerates also restrain the oxygen transport.[8, 97, 103, 110-114]

Besides hindering oxygen transport resulting in performance loss, these structural heterogeneities caused by the ionomer also lower the PGM utilization.[112, 115-116]

To reduce mass transport resistance in the CLs, one strategy is to precisely control the CL hierarchical structure. Although novel designs of CL local structure have been proved to enhance the CL transport properties and PGM utilization, understanding on the formation of the global structure and the origin of heterogeneous structural characteristics are still missing.[14, 97, 108]

2.6 Summary

There are extensive computational and experimental researches focusing on the structural correlation between catalyst inks and CLs, which provide valuable information on the static components and evolution of the particulate structure in the catalyst ink. There is also good amount of evidence and analysis pointing to the heterogeneous hierarchical particulate structure of the CL for being responsible for the mass transport resistance, especially oxygen transport resistance. However, a principled framework for understanding the formation-structure-process-functionality relationship of the CLs has been missing.

Firstly, regarding the formation of the particulate structure, current understanding on the ink-CL structural translation through CL fabrication process is limited to solidification, leaving the shear involved in the process overlooked. Moreover, in no instance the formation process of the hierarchical particulate structure or the origin of heterogeneous characteristics of the particulate structure have been experimentally investigated with respect to CL fabrication process. Additionally, understanding of the underlying physics on how the ink design parameters affect CL structure that provides electrochemical and transport properties is lacking as well. Also, it was not clear in the literature how the time-sensitivity of the particulate structure in the catalyst through the CL fabrication process was taken care of. Considering the delicacy and dynamics of the particulate structure in the catalyst ink, very few experimental methods are non-destructive to the particulate structure.

Herein, this research qualitatively addresses the abovementioned issues by focusing on the translation of the supported catalyst-ionomer particulate structure from a hierarchical holistic physical point of view. The experiments were designed with respect to the CL fabrication process in a time-controlled and shear-controlled manner to capture the key aspects of the particulate structure formation process. With standard materials (Pt/C, PFSA, and water/IPA), non-destructive methods based on colloidal suspension and complex fluid were employed to investigate the

local and global structure of the ionomer-supported catalyst assemblage in the catalyst ink.

The first part of the research attempts to elucidate the formation process of the CL hierarchical structure, explores the origin of the multiscale structural heterogeneity, and studies the role of water/IPA ratio in the structure formation process. A bottom-up approach was employed to qualitatively investigate the hierarchical structural assemblage of the CL constituent materials inside the catalyst ink and the structural translation into pristine CLs through shear process. Specifically, the ionomer conformation and interaction with the Pt/C surfaces in the catalyst inks and the structure translation of the ionomer-Pt/C assemblage through shear into pristine CLs, depending on the water/IPA ratio, were investigated.

Then, the effect of I/C ratio and solid content on the ionomer-supported catalyst assemblage were systematically studied to establish a formulation-structure-functionality relationship with fundamental understanding. Based on the framework and approach from the first part, this part of the research qualitatively explores the compound effect of the I/C ratio and the solid content on the formation-structure-functionality relationship of the CLs. The objective in this part was twofold: 1) to elucidate the roles of the I/C ratio and the solid content in the formation of the CL microstructure and 2) to demonstrate the compound effect of the I/C ratio and the solid content on the mass transport, in particular the oxygen transport.

CHAPTER 3

EXPERIMENTS

Considering the shear involved in the CL fabrication process and the dynamic nature of the catalyst ink, measurements best capturing the particle dynamics in the catalyst ink and non-destructively characterizing the shear influence on the ink microstructure are required.

3.1 Particle characterization

Since the catalyst ink is a colloid dispersion of CL constituent materials, the particle dynamics can be captured by dynamic light scattering, which non-invasively measures the diffusion coefficient of particles undergoing Brownian motion in the liquid medium. The size of the particles, which is the hydrodynamic diameter, is related to the diffusion coefficient via Stoke-Einstein equation (Eq. 3.1),

$$d_H = \frac{k_B T}{3\pi\eta D}$$
(3.1)

where d_H is hydrodynamic diameter, k_B is Boltzmann's constant, T is the absolute temperature, η is the viscosity of the medium and D is the diffusion coefficient. The hydrodynamic diameter of a particle includes the hydration effect, which is suitable for studying the CL constituent materials in the catalyst ink. The value of hydrodynamic diameter depends on molecular weight, specific refractive index increment, electrostatic interactions, particle size, measurement angle, laser wavelength, sample concentration, the surface structure, particle shape, and solution ionic strength.[117] Note that the Brownian motion of the particles in a certain liquid medium can be affected by the particle concentration or interparticle distance. Namely, this measurement is sensitive to particle concentration. Four concentration-dependent effects can manifest the results, including multiple scattering, restricted diffusion, reversible self-association, and electrostatic repulsion. When the system is very dilute or the particles are far, the measured diffusion coefficients or the derived hydrodynamic sizes are representative of the particles in the sample. Therefore, this measurement is usually carried out with dilute samples.

In this research, the size distribution of the particles from the catalyst inks was used to study the interaction between the ionomer and Pt/C nanoparticles. The measurements were carried out in corresponding dilutions at room temperature

with a Zetasizer Nano ZS90 from Malvern. A consistent small volume of each ink sample was diluted into 5 mL of its corresponding dispersing medium and then sonicated for 10 minutes. 1 mL of the diluted sample was used in each measurement. A dip-cell was employed for electrophoretic mobility measurement. In addition to size distribution, the electrophoretic mobility was also measuring to approximate surface charge through electrophoresis light scattering performed on the same instrument with the same sample.

3.2 Rheological measurements

Rheology is the study of deformation of matters. By controlling stress/strain imposed on the sample as the input, structural response in terms of strain/stress from the measured sample is collected. Considering the catalyst ink go through a shear deformation during ink processing. Rheology is very suitable for monitoring the structural dynamics quantitatively throughout a defined processing condition. The basic idea of applying rheology in this work is to characterize the intact ink microstructure and to describe the structural deformation induced by a simulated coating process. Along the ink processing, intact ink structure, structural response to shear deformation, and flow property are characterized by small amplitude oscillation shear and steady-state shear rump, respectively. By holding certain amount of the sample in between a pair of parallel plate geometry, a rotational thin disk flow will be achieved (the bottom plate is fixed in our case, Figure 3.1). Rheological measurements based on such a flow can be easily carried out.
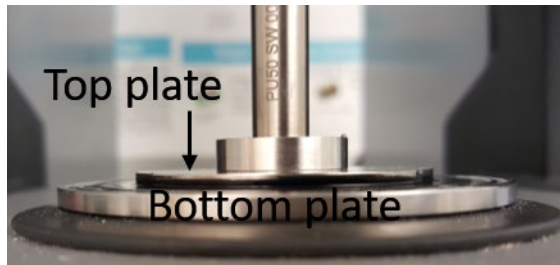
Figure 3.1: A parallel-plate geometry for rheological measurements.

Oscillation test is typically used to characterize the viscoelastic properties of the matter. Catalyst inks consist of solid spherical particles and polymeric electrolyte are typical viscoelastic materials, which exhibits both elastic and viscous characters. The microstructure of the catalyst inks was therefore characterized by oscillatory tests, where a sinusoidal displacement is applied to the top plate (Eq. 3.2).

$$x_p(t) = x_{p,0} \sin \omega t \tag{3.2}$$

where x_p is the applied displacement, $x_{p,0}$ is the displacement amplitude, ω is angular frequency, and t is the time. The resulting strain, γ , can be calculated by Eq. 3.3:

$$\gamma(t) = \frac{x_p(t)}{h} = \frac{x_{p,0}}{h} \sin \omega t = \gamma_0 \sin \omega t \tag{3.3}$$

where h is the predetermined gap between the top and bottom plate geometry and γ_0 is the strain amplitude. If the strain amplitude γ_0 is small enough (typically $\gamma_0 \ll 1$), the structure of the sample remain undisturbed by the deformation[118]. The measured stress is controlled by the rate of spontaneous rearrangement of the sample structure at equilibrium. The stress produced by a small amplitude oscillatory shear is in proportional to the applied strain amplitude and varies sinusoidally with time (Eq. 3.4).

$$\tau(t) = \gamma_0 [G'(\omega) \sin \omega t + G''(\omega) \cos \omega t] \tag{3.4}$$

where G' is the elastic modulus, G'' is the viscous modulus. G' represents storage of the elastic energy while G'' represents the viscous dissipation of the elastic energy. When $G' >> G''$, the material is solid-like. When $G' \ll G''$, the material is liquid-like. The regime where the stress can be expressed by Eq. 3.4 is called the linear viscoelastic regime. The maximum strain of this regime is considered as the critical strain, γ_c, beyond which the structure is considered out of the equilibrium.

In this work, small amplitude oscillatory shear was employed since it works within the linear viscoelastic region and thus does not significantly destroy the microstructure of sample. According to Eq. 3.4, the microstructure of catalyst inks can be characterized as a function of strain amplitude (γ_0), frequency ($f = \omega/2\pi$) and time, respectively.

The intact ink microstructure was characterized by amplitude sweep and frequency sweep. Amplitude sweep test was firstly performed to determine the sample critical strain, γ_c. During an amplitude sweep, the amplitude varies while keeping the frequency constant. Within the linear viscoelastic regime, the shear moduli remain constant. In our measurements, the critical strain is defined as the strain where the elastic modulus deviates 5 % from its linearity. After defining the critical strain, a frequency sweep test was then performed within the linear viscoelastic region to probe the microstructure in the ink. During a frequency sweep, the shear strain amplitude remains constant ($< \gamma_c$) while the frequency changes. When $G' > G''$ and G' is independent of frequency, a gel structure of the dispersed particles is expected.

To characterize the structural change due to shear deformation from coating, a simulated coating process (explained below) was applied in the middle of time

sweep test. The time sweep test was performed within the linear viscoelastic region to observe the microstructural response to the simulated shear. During the time sweep, both the frequency and strain amplitude are kept constant. Since the G' represents more closely to the ink network, change of G' against time was recorded.

Steady-state flow behavior of the catalyst inks were characterized by measuring viscosity-shear rate plot. A time-controlled shear rate logarithm ramp from 0.01 1/s to 1000 1/s at the frequency of 1 Hz was performed. The shear rate of coating a thin film CL in real application is typically above 500 1/s to increase throughput. In this study, a shear rate of 1000 1/s was used to simulate the shear deformation during the coating process.

All the rheological measurements were performed on a high-resolution rotational rheometer (Kinexus Ultra+, Malvern) equipped with a Peltier temperature controller at 25.00 ± 0.02°C. Based on the particle size measured by dynamic light scattering, a constant gap of 250 μm was controlled between the top and bottom plates. Considering the intact structure of the catalyst inks are sensitive to shear history, the samples were handled in the same manner. After mixing, the samples were carefully loaded onto the bottom geometry using a spatula. Then the top geometry was lowered towards the bottom geometry at a very slow speed to prevent changing the microstructure of the ink. After the gap of 250 μm is reached, the sample was then stabilized for 10 minutes prior to the measurements. All samples were prepared and measured following the same processes. Roughened parallel plates (dia. 40 mm) with solvent trap were used to minimize the wall slip effect and solvent evaporation.

3.3 Fluorine-19 nuclear magnetic resonance spectroscopy

Fluorine-19 nuclear magnetic resonance (^{19}F NMR) were used to carry out measurements for Ionomer chain mobility in the dispersions. The measurements were carried out on Agilent ProPulse 500 MHz NMR system with samples that contain the same amount of all the materials except for Pt/C. Data analysis and fitting was assisted by OriginPro.

3.4 Field emission scanning electron microscopy

CLs were manually coated on a piece of ETFE substrate from the catalyst inks using various formed Mayer rods for catalyst loading control, then dried under gentle ventilation at room temperature. The coating process was done at a shear rate of 1000 1/s. The structural characteristics of the CLs were observed using a field emission scanning electron microscope (Gemini 500, Zeiss) operating at 500 V to avoid ionomer melting.

3.5 Fuel cell operation

Membrane electrode assemblies (MEAs) were prepared as followed. The anodes were prepared by coating a CL onto the gas diffusion layer (H23C8, Freudenberg) with Pt loading of 0.3 mg_{Pt}/cm^2_{geo}. The cathodes were prepared by decal transferring the prepared CLs onto a piece of Nafion membrane (NR-211, Dupont) at 140°C with Gylon protectors under a pressure of 300 psi for 10 minutes. The Pt loadings of the cathodic CLs were determined by weight measurements to be 0.2 mg_{Pt}/cm^2_{geo}. The active areas were 2 cm^2. Each prepared MEA was then assembled into a single-cell hardware (Fuel Cell Technology Inc.).

Fuel cell tests were performed on a precise-controlled automated fuel cell test station (Greenlight Innovation). Electrochemical measurements were performed using a potentiostat (Reference 3000, Gamry) with a 30 k booster. The detailed test protocols are listed in Table 3.1. Prior to the tests, all MEAs were firstly inspected by a cyclic voltammetry (CV) measurement for the initial electrochemically active surface area (ECSA) and then conditioned to steady state by cycling a voltage-controlled procedure sequence, which includes 0.6 V for 15 minutes, 0.85 V for 15 minutes, and open cell voltage (OCV) for 5 minutes. The current density of each data point on the polarization curve were averaged over the last minute. High frequency resistance data were collected at each polarization data point by AC impedance operating at 10,000 Hz.

3.6 Fuel cell diagnosis

To approximate the reaction site density, ECSA of each cathode was evaluated through CV scanning at 50 mV/s.[110, 119-120]

The proton transport resistance in the cathode, R_{H^+}, was determined by AC impedance measuring from 100 kHz to 0.1 Hz. The measurements were performed under differential flow condition, which maintains constant gas partial pressure in the flow channels resulting in unchanged relative humidity (RH), since the proton transport is sensitive to the RH.[25]

The pressure-dependent and pressure-independent oxygen transport resistances, $R_{O_2}^{p,d}$ and $R_{O_2}^{p,i}$, were extracted from dry limiting current measurements.[26, 29, 121] Note that $R_{O_2}^{p,d}$ in this study excludes the transport resistance in the flow channels and corresponds to the value measured at 300 kPa. The dry mole fraction of oxygen ranges from 1% to 4%.

Table 3.1. Fuel cell test protocols.

Test	Temp. (°C)	Gas (an/ca)	Pressure (kPa)	RH (%)	Flow rate (an/ca, L/min)	Load control	Step hold time (min)
Dry polarization	70	H_2/Air	300	64	0.4/0.2	OCV-0.2 V	10
Wet polarization	70	H_2/Air	300	100	0.4/0.2	OCV-0.2 V	10
CV	30	H_2/N_2	100	100	0.02/0.04	1.2-0.1 V	N/A
EIS	60	H_2/N_2	300	100	0.1/0.1	0.2 V DC w/ 10 mV AC	N/A
Dry limiting current	80	H_2/Air & N_2	100, 150, 200, 300	64	0.4/0.2	0.3-0.09 V	2

CHAPTER 4

HIERARCHICAL STRUCTURE OF THE CATALYST LAYER

Dispersing medium has a very profound impact on the ink property. It governs the ionomer conformation, the size distribution of inorganic nanoparticles and the interaction between ionomer and nanoparticles.

In the lights of the underlying physics, this chapter attempts to elucidate the formation process of the CL hierarchical structure and explores the origin of the multiscale structural heterogeneity. A bottom-up approach is employed to qualitatively investigate the hierarchical structural assemblage of the CL constituent materials inside the catalyst ink and the structural translation into pristine CLs through shear process. Specifically, the ionomer conformation and interaction with the Pt/C surfaces in the catalyst inks and the structure translation of the ionomer-Pt/C assemblage through shear into pristine CLs, depending on the liquid medium, are investigated using fluorine-19 nuclear magnetic resonance (^{19}F NMR), dynamic light scattering, rheological measurements, and field emission scanning electron microscopy. The results suggest that besides the shear process, the structure of the hierarchical assemblage of the CL constituent materials, depending on the chemical environments, plays a critical role in determining the heterogeneous CL structure.

The catalyst inks were made of Pt/C (40 wt.% Pt, JM HiSPEC 4000), PFSA ionomer (20 wt.% Nafion, Dupont D2020) and water-isopropanol alcohol (IPA, HPLC grade, Sigma Aldrich) binary solvent. The carbon volume fraction and ionomer concentration were set at 3.5 v.% and 61.5 mg/mL liquid, respectively. Two catalyst inks were studied by controlling the volume fraction of IPA ($\emptyset_{IPA}$) in the binary mixture denoted as water-rich ($\emptyset_{IPA}$= 0.25) and IPA-rich ($\emptyset_{IPA}$= 0.75) systems. For only size distribution and electrophoretic measurements, 2 mg of catalyst inks and component dispersions were diluted into 5 mL of corresponding dispersing medium, respectively.

4.1 The conformation of ionomer aggregates—mobility of the ionomer chains

The conformation of the ionomer in the water/alcohol mixture was probed in terms of chain mobility. With known ionomer molecular structure (Figure 4.1a), liquid composition, and ionomer concentration, the chain mobility can be primarily attributed to the segmental motion of the ionomer chains. Since the only difference

among these samples in this study is the volume fraction of IPA in the solvent, the chain motion is hence merely affected by the chemical environment.
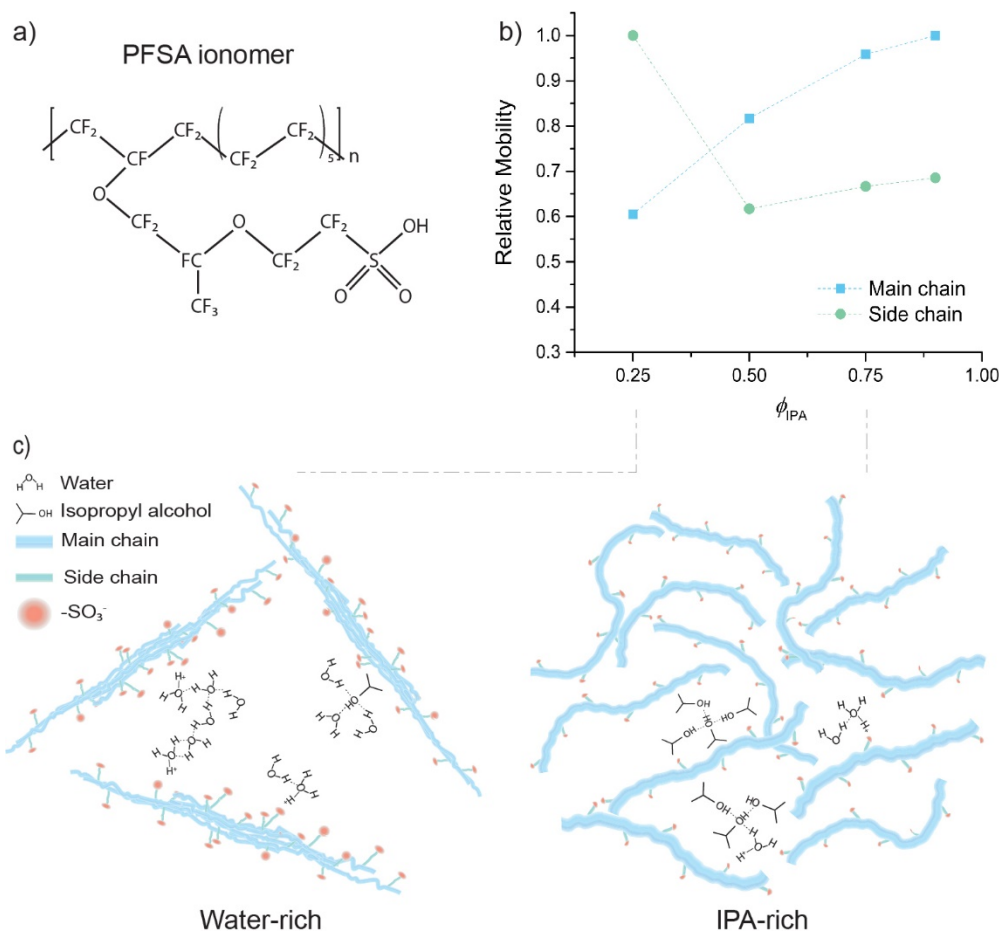
Figure 4.1. a) The chemical structure and b) chain mobility dependence of perfluorosulfonic acid (PFSA) ionomer on isopropyl alcohol volume fraction ($\emptyset_{IPA}$) in IPA aqueous solutions. c) Schematic diagrams of potential ionomer conformations in water-rich ($\emptyset_{IPA}= 0.25$) and IPA-rich ($\emptyset_{IPA}= 0.75$) dispersing media, respectively.

The mobilities of PFSA ionomer main chain and side chain in various water-IPA mixture are presented in Figure 4.1b. For clarity, both the values of the main-chain mobility and the side-chain mobility have been normalized against the highest value from the original results. The normalized result shows that both the main chain mobility and the side chain mobility drastically depend on the alcohol volume fraction, $\emptyset_{IPA}$. As $\emptyset_{IPA}$ increases, the value of the main-chain mobility

inclines significantly over 50% from water-rich system ($\emptyset_{IPA} = 0.25$) to IPA-rich system ($\emptyset_{IPA} = 0.75$); meanwhile, the value of the side-chain mobility declines about one third from the water-rich environment to the IPA-rich with a minimal value occurring around $\emptyset_{IPA} = 0.5$. The minimal value of the ionomer side-chain mobility is considered to be the result of relatively low free water molecules due to stronger hydrogen bonding between the IPA and the water.

Theoretically, the two chemical environments have different affinities to the ionomer main chain and side chain, respectively. The affinity of the chemical environment to the ionomer chain is often predicted by the similarity between their solubility parameters, i.e. Hildebrand solubility parameter and more specifically Hansen solubility parameters, that are associated with their cohesive energy densities [122]. The relationship between Hildebrand solubility parameter and Hansen solubility parameters are described in the following equations:

$$\delta^2 = E/V \tag{4.1}$$

$$E/V = E_D/V + E_P/V + E_H/V \tag{4.2}$$

$$\delta^2 = \delta_D^2 + \delta_P^2 + \delta_H^2 \tag{4.3}$$

where δ is the Hildebrand solubility parameter, E is the cohesion energy density, V is molar volume; δ_D, δ_P and δ_H are the components of Hansen solubility parameters, representing the dispersive, polar, and hydrogen-bonding cohesive energy density, respectively. The solubility parameters of the ionomer and the two chemical environments and their differences are listed in Table 4.1. According to the Hildebrand solubility parameters, the water-rich environment is relatively suitable for the ionomer side chain, but much less compatible with the PFSA ionomer main chain. This can lead to strong aggregation of the hydrophobic perfluoro main chain. Contrastingly, the IPA-rich environment has higher affinity to the ionomer main chain indicating better dispersity of the main chain. Further, as indicated by the Hansen solubility parameters, there exists strong polar interaction between the ionomer and the water-rich environment which can lead to high extent of ionization of the sulfonate groups at the side chains. However, the strong hydrogen bonding in the water-rich environment can cause thick solvation shell preventing the side chains them from clustering electrostatically. Whereas both the ionization and solvation effects can be expected to be weaker in the IPA-rich environment.

Table 4.1. Solubility parameters of PFSA ionomer and the IPA aqueous solutions.

Solubility parameters ($MPa^{0.5}$)	PFSA Ionomer	Water-rich	IPA-rich
δ	19.8[m]/35.4[s]	38.4	28.3
δ_D	17.4	15.6	15.8
δ_P	12.5	12.4	8.30
δ_H	9.6	32.8	22.0
$|\Delta\delta|$	-	18.6/3.00	8.50/7.10
$|\Delta\delta_D|$	-	1.80	1.60
$|\Delta\delta_P|$	-	0.10	4.20
$|\Delta\delta_H|$	-	23.2	12.4

[m]. PFSA ionomer main chain.
[s]. PFSA ionomer side chain.

Besides the chemical environment, the structure and morphology of PFSA ionomer can also be affected by the concentrations of the ionomer. It was reported that PFSA ionomer main chains aggregate into bundle-like primary aggregates at very dilute concentration below 0.2 mg/mL.[42, 92, 123] Then the primary PFSA ionomer bundles start to aggregate electrostatically through the sulfonate groups from the side chains at a concentration around 1.0 mg/mL (MeOH/H_2O = 4 : 1 wt.), disordered segments of the main chains from the bundles start to overlap at a concentration around 5.0 mg/mL (MeOH/H_2O = 4 : 1 wt.), and no liquid flowing about at 20 v.% (IPA/H_2O = 1 : 1 v.).[42, 67, 123] Although these studies were performed in various chemical environments, the values of these concentrations seem to be consistent. The concentration used in this study is slightly higher than the overlapping concentration where ionomer bundles with overlapped chain segments can be expected.[124]

With the consideration of the role of the chemical environment and the concentration, the conformation of the ionomer aggregates can be conjectured based on the mobility data as following. In the water-rich environment, the ionomer main chains aggregate strongly into stiff bundle-like primary aggregates. Whilst the side chains are highly ionized with thick solvation shell that leads to limited electrostatic clustering due to screening effect.[125] Such large difference in the mobilities of main chain and side chain can lead to strong segregation of the

25

hydrophobic and hydrophilic domains.[126] Due to the concentration effect, the main chains of the ionomer overlap with each other forming secondary aggregates, the ionomer may exhibit conformation of highly swelled side chains with compactly packed main chains. which agrees with observation from cryo-TEM and coarse-grained molecular dynamic simulation.[124, 127] However, in the IPA-rich environment, the ionomer main chain appears to be dispersed as the primary particles. The sides chains are weakly ionized due to lower dielectric constant (64.9 for water-rich solvent and 31.7 for IPA-rich solvent) as a result of low similarity to the polar interaction for dissociation of sulfonate acid. Thin solvation shell can be expected which leads to electrostatic clustering of the sulfonate group from the side chains forming secondary particles. This agrees with the observation of TEM in the literature.[42] A schematic of the hypothetic ionomer structures in both water-rich and IPA-rich environments are illustrated in Figure 4.1c. The conformations of the ionomer chains are proposed based on the simulation results of the rigidity of the chains of the ionomer in the literature.[124, 128]

4.2 The hierarchical assemblage of the ionomer and Pt/C nanoparticles in dilute system—ionomer interactions with Pt/C nanoparticles

The interactions between the ionomer and the Pt/C nanoparticles in the water-rich and IPA-rich environments were investigated in a dilute by observing the change of the hydrodynamic diameter distribution of Pt/C nanoparticles caused by the presence of the ionomer aggregates. The hydrodynamic diameter is defined as the diameter of a sphere that diffuses at the same speed as the particle being measured.[129-131] The interactions between the ionomer and the carbon were also investigated. The results are shown in Figure 4.2.

In the water-rich environment, the presence of the ionomer induces interparticle association to both carbon and Pt/C systems. As shown in Figure 4.2a, the presence of water-rich ionomer causes evident peak broadening with the size distribution of carbon particles spanning from 233.4 ± 55.42 nm to 335.8 ± 127.3 nm. The broadened peak with a similar lower limit indicates weak destabilization of the carbon particles due to the presence of the ionomer. Such a phenomenon can be ascribed to the surface effect of the aggregated ionomer backbone on the carbon particles, i.e. primarily patching via being adsorbed on most of the outer surface of carbon particles and partially bridging via being confined in between the carbon surfaces.[71, 73, 78, 132] This is supported by the electrophoretic mobility data shown in Appendix. Consequently, the presence of the ionomer adds complexity to the structure of the carbon particles. On one hand, due to rapid adsorption, the non-uniformly distributed ionomer can lead to densified particle structure, which has been reported in a closely similar system

26

that the mass fractal dimension of both carbon aggregates and agglomerates increases from 3.08 to 3.20 and from 2.25 to 3.13 respectively.[67-68, 70] On the other, the bridging effect or the interparticle association promotes the formation of larger agglomerates.[80, 133] When Pt also presents (Figure 4.2b), a similar phenomenon can be observed with the size distribution extending from 252.9 ± 50.7 nm to 346.6 ± 120.8 nm. However, due to a significant decrease of the ionomer adsorption rate caused by the presence of Pt, the formation of more inhomogeneous particle local and global structure and potentially existence of free ionomer in the system can be expected.[68, 78]
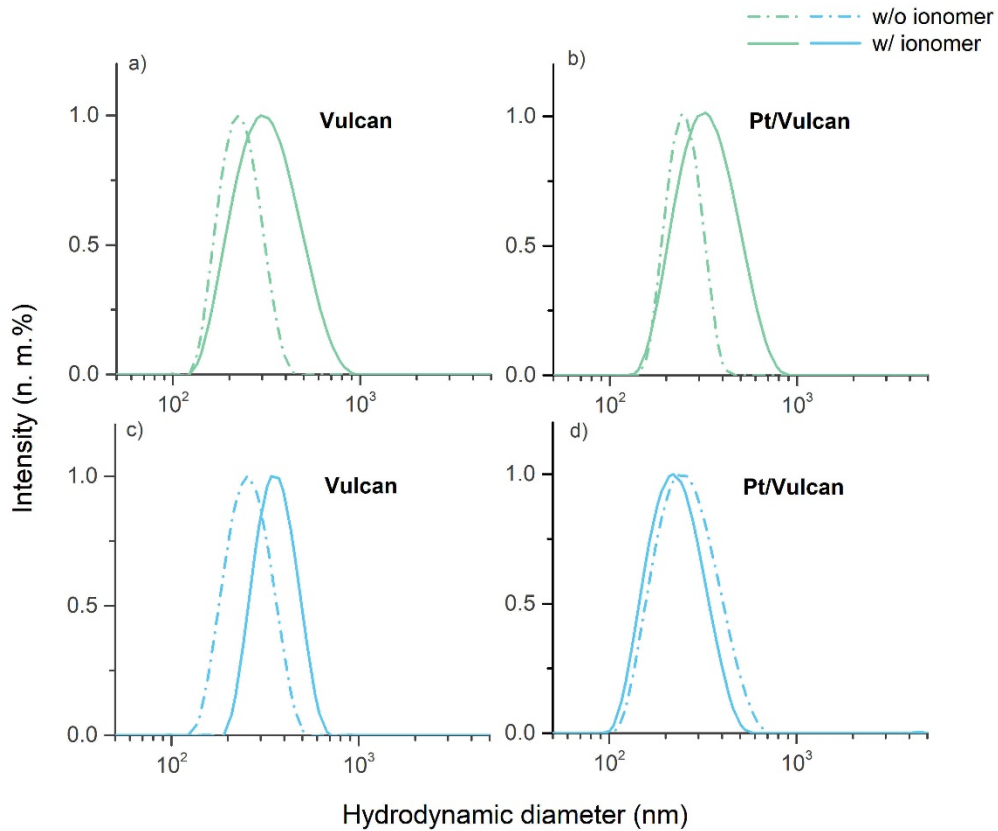
Figure 4.2. Hydrodynamic diameter of (a and c) carbon particles and (b and d) Pt/C particles, (dash dot) without and (solid) with ionomer, in (a and b) water-rich and (c and d) IPA-rich dispersions, respectively.

In the IPA-rich environment, ionomer causes seemingly distinct interactions with carbon and Pt/C systems, respectively. As shown in Figure 4.2c, the presence of the ionomer shifted the size distribution of carbon particles from 264.9 ± 69.48

nm to 368.4 $\pm$ 88.22 nm, with a coarser lower limit and slightly narrowed peak. The observed phenomenon can be attributed to the surface effect of the non-aggregated bent ionomer backbone on the carbon particles, i.e. mainly patching via being adsorbed on most of the entire surface of the carbon particles and rarely bridging via being confined in between the carbon surfaces.[67, 71, 128] The unlikely bridging effect in this case lies in the difficult aggregation of ionomer backbones. The adsorption, on the other hand, is greatly favored and consequently leads to both densification of the finest particles and steric repulsion in between these particles. The result is a finely flocculated but well dispersed particulate system, which is supported by the drastically decreased mass fractal dimension (from about 3.3 to 1.5) shown in a closely similar system.[72] Distinguished from the carbon system, when Pt presents as shown in Figure 4.2d, the size distribution of the particles shifted to a slightly finer direction from 272.0 $\pm$ 97.86 nm to 236.4 $\pm$ 76.60 nm. This phenomenon signals accelerated diffusion of the suspending particles usually due to enhanced interparticle repulsion. Such repulsion can be attributed to the interaction between ionomer sulfonate groups and Pt surface.[134]

Consequently, the release of ionic moieties and the adsorption of ionomer due to interaction with Pt can result in entropic and steric repulsion, respectively. The electrophoretic mobility data in Appendix and the decreased mass fractal dimension in a closely similar system support this scenario.[72] Therefore, with the presence of Pt a highly dispersed particulate system with finest flocs can be expected.

In summary, the ionomer-Pt/C assemblages formed in water-rich and IPA-rich environment appear to have quite distinct structures. The former tends to form a coarsely densified and attractive structure with ionomer adsorbed at the outer surface, while the later tends to form finely densified and repulsive structure that ionomer possibly covers the entire surface area. Such distinguishable structural characteristics will play a critical role in both the growth and evolution of the particulate structure—the pristine CL microstructure.

4.3 The intact structure of ionomer-Pt/C assemblage in concentrated systems—catalyst inks

This section aims to elucidate the structure of the ionomer-Pt/C assemblage at higher concentration in the form of catalyst inks. The degree of the structural growth of the ionomer-Pt/C assemblages in water-rich and IPA-rich environment were investigated by measuring phase-related linear viscoelastic properties of the dispersions of inorganic particles without and with ionomer respectively.[135] The results are shown in Figure 4.3. For clarity, the results of ionomer samples are shown in the Appendix.
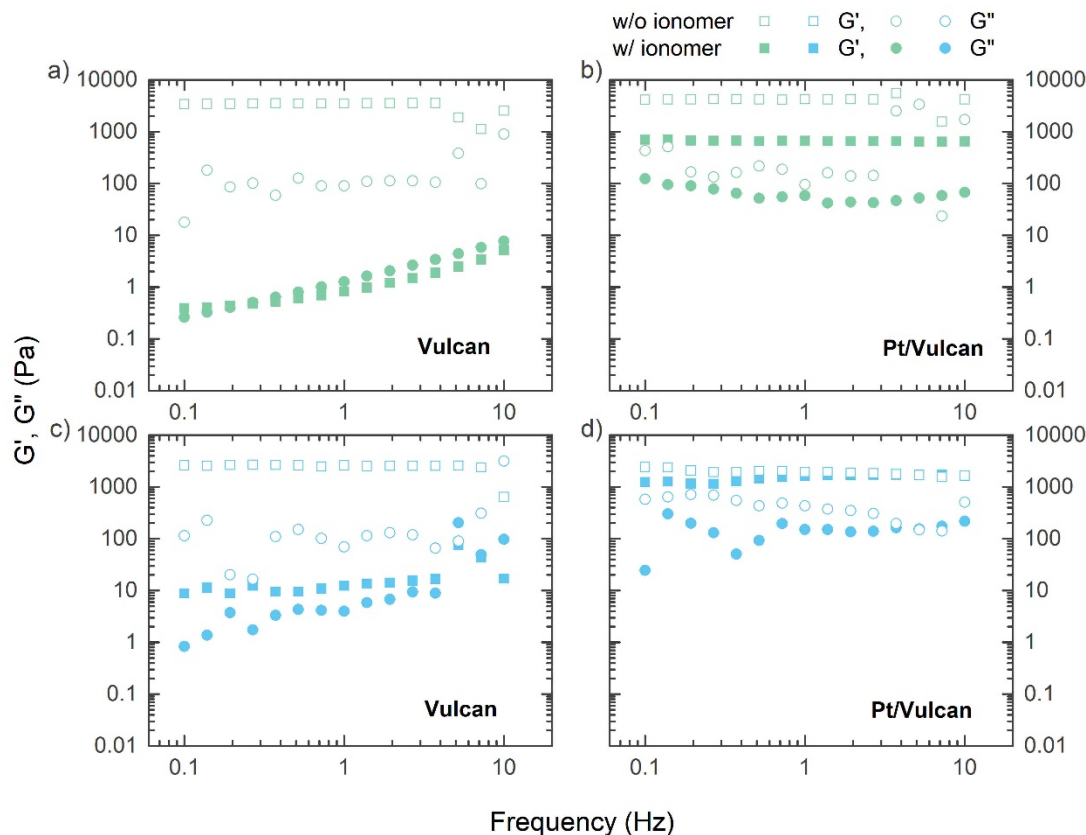
Figure 4.3. Frequency-dependent linear viscoelastic properties of concentrated (a and c) carbon aggregates and (b and d) Pt/C aggregates, (open) without and (solid) with ionomer, in (a and b) water-rich and (c and d) IPA-rich liquid medium, respectively. Squares are for elastic modulus, G' and circle are for viscous modulus, G". The carbon volume fractions and the ionomer concentrations in liquid phase remain the same in all the samples.

In the water-rich environment, the structures of the ionomer-carbon and the ionomer-Pt/C assemblage seem to be rather distinguishable exhibiting distinct linear viscoelastic properties. As shown in Figure 4.3a, the carbon particle dispersion has a nearly constant elastic modulus, G', which is greater than the viscous modulus, G'', demonstrating the viscoelastic characteristics of the space-filling structure, gel.[118] However, the presence of the ionomer brings a drastic change to the gel behavior or the carbon system, as G'' is more dominant than G' with a crossover at about 0.3 Hz. This result suggests rare crosslinking in the structure with discrete substructures that have a relatively long relaxation time. Recalling that the ionomer-carbon system is attractive and tends to coarsely densify, the discrete substructures can be attributed to dense clusters formed in the system

and potentially with large sizes. When Pt presents at carbon surface, the average value of G' increases as shown in Figure 4.3b. With the presence of ionomer, the space-filling structure of the Pt/C particles remains but with a lower average value of G', suggesting decreased structural crosslinking which can be attributed to the adsorption of ionomer onto Pt/C particles forming clusters that is relatively small compared to the ionomer-carbon ones. This is supported by the reported mass fractal dimension value is 3.13 for the ionomer-carbon clusters and around 1.4 for the ionomer-Pt/C clusters.[70, 74] The evident difference between the cluster structure formed in the ionomer-carbon system and in the ionomer-Pt/C system can be attributed to the presence of Pt at carbon surface, which adds roughness to the carbon surface forming finer structure.[136]

In the IPA-rich situation, the structural difference between the ionomer-carbon and the ionomer-Pt/C assemblage seems to be not far. As shown in Figure 4.3c, the presence of the ionomer on carbon causes the formation of a space-filling structure as the G' of the ionomer-carbon system is dominating and nearly constant. The low average value of the G' of the ionomer-carbon system can be attributed to the densification of fine particles and the entropic repulsion in between. When Pt also presents, shown in Figure 4.4d, the structural crosslinking increased significantly as the average value of the G' is very close to that of the Pt/C particle suspension. The change in the structure can be attributed to weak repulsion between fine ionomer-Pt/C particles as a result of Pt presence which increase ionomer adsorption and surface roughness.

At high concentration, both the ionomer-Pt/C assemblages in water-rich and IPA-rich catalyst inks grow into space-filling gels. The gel structure of ionomer-Pt/C assemblages grows from varisized dense clusters in the water-rich system and fine repulsive clusters in the IPA-rich system. Note that the surface roughening effect caused by the presence of Pt seems to become prominent on the structure of the ionomer-Pt/C assemblage.

4.4 The shear response of the ionomer-Pt/C assemblage in the catalyst ink

In practice, the ionomer-Pt/C assemblage in the catalyst ink is constantly exposed to shear. Hence, profiling the shear response of the ionomer-Pt/C assemblages in the catalyst ink is critical. The shear profiles of the ionomer-Pt/C assemblages in the water-rich and the IPA-rich catalyst inks are shown in Figure 4.4. Here the contribution of the ink solvent to the measured shear properties are considered to be negligible. As seen in Figure 4.4a, both samples exhibit non-linear or non-Newtonian nature indicating the complexity of the inner structures, as their viscosities change nonlinearly with the shear rate as seen in Figure 4.4a. Such non-

Newtonian behavior of these structures can be empirically described by the Herschel-Bulkley model:[137]

$$\tau = \tau_0 + k\dot{\gamma}^n \qquad (4.4)$$

where τ_0 is yield stress (Pa), k is consistency index (Pa s^n), n is flow index, $\dot{\gamma}$ is the shear rate (1/s), and τ is the shear stress (Pa). The measured $\tau - \dot{\gamma}$ plots and the model fitting results of the two samples are further shown in Table 4.2 and Figure 4.4b, respectively.

Table 4.2. Herschel-Bulkley model fitting results.

	τ_0 (Pa)	k(Pa s^n)	n	R^2
Water-rich	11.6	0.923	0.650	0.99997
IPA-rich	41.4	1.749	0.612	0.99945

In the water-rich catalyst ink, when the shear rate is less than 0.03 1/s the ionomer-Pt/C assemblage exhibit a yield stress of 11.6 Pa (Figure 4.4a) resisting the shear motion and showing a viscosity plateau (Figure 4.4b). The shear resistance can be attributed to the Brownian motion of the structural building blocks where yield stress is required to overcome the interparticle forces trapping the particles [86, 118]. When the shear rate is larger than 0.03 1/s, the structure of the ionomer-Pt/C assemblage starts to flow and stress is required to sustain the shear motion of the structure, i.e. the rearrangement and alignment of the structural building blocks with the shear plane. In this power law region, the ionomer-Pt/C assemblage exhibits a shear-thinning nature, as the viscosity decreases exponentially with the shear rate. As seen in Table 4.2, the value of n is less than one verifying the shear-thinning behavior of the structure. The k value is the proportionality of the power law region. A low value means the ease to maintain the flow, equivalent to low structural crosslinking. The shear-thinning behavior is desirable for catalyst ink processing, as it allows the spreading of catalyst inks into thin films.
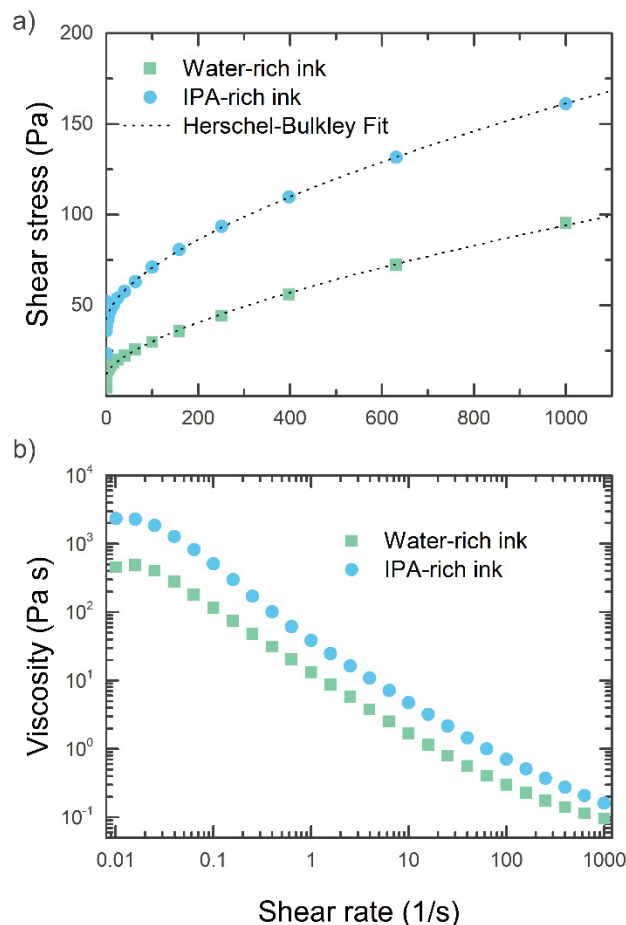
Figure 4.4. a) Steady shear behavior curves of the water-rich and IPA-rich catalyst inks. Dot lines are Herschel-Bulkley model fit to data. b) Viscosity as a function of shear rate for the water-rich and IPA-rich catalyst inks.

While in the IPA-rich catalyst ink, the ionomer-Pt/C assemblage exhibits a yield stress of 41.4 Pa in the Brownian region resisting against the shear flow with Brownian viscosity being five times higher than the water-rich one. Strong interparticle forces can be expected. As suggested by the values of k and n in the Table 4.2, the ionomer-Pt/C assemblage has relatively high extent of structural crosslinking and spreadability which can be beneficial in high shear processing.

High shear processing is commonly employed in transforming catalyst inks into CLs. During such a process, the ionomer-Pt/C assemblage in the catalyst ink is exposed to shear which provides external hydrodynamic force field promoting the motion of the structure building blocks. The implementation of shear exits once the wet thin film of pristine CL is deposited. The corresponding structural response

of the ionomer-Pt/C assemblage from the catalyst ink can play a critical role in the formation of the microstructure of the CL. To investigate the shear-induced structural dynamics of the ionomer-Pt/C assemblage, a high shear process was simulated as followed. Following a non-disturbing condition, a shear rate of 1000 1/s is implemented for 10 s, since the typical shear rate of coating process is about 1000 1/s or even higher.[15, 49, 138] Then the shear was removed to observe the time-dependent shear-free response of the ionomer-Pt/C assemblages from the catalyst ink for 300 s. For clarity, the results were normalized based on the shear-thinning behavior and shown in Figure 4.5.
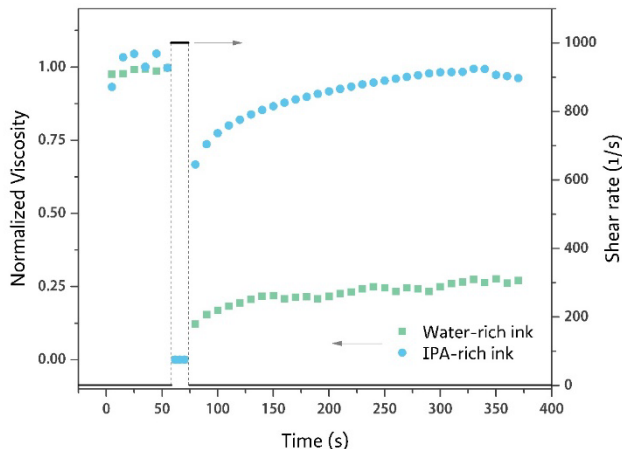
Figure 4.5. Time-dependent oscillatory viscosities of water-rich and IPA-rich inks in response to the simulated processing condition, 1000 1/s for 10 s.

Surprisingly, the ionomer-Pt/C assemblies in the water-rich and IPA-rich catalyst ink exhibit distinguishable profiles of shear-induced time-dependent response after the removal of the shear. 300 s after the removal, the shear resistance of the rearranged ionomer-Pt/C assembly from the water-rich ink reaches 24.9% of the original. At the meantime, the ionomer-Pt/C assemblies from the IPA-rich ink has contrastingly recovered 98.2% of the shear resistance, which suggests a thixotropic nature.[139] Shear resistance is important to the structure of the ionomer-Pt/C assemblies as it prevents the breakage of the percolating network and collapse of the pores in the pristine CL. With the chemical environment being the only variable in forming these two systems, such prominent difference in the structural shear resistance needs to be further understood.

The time-dependent G' of the two samples after the shear removal are presented in Figure 4.6. As seen, the simulated shear process causes significant loss

to the structural crosslinking of the ionomer-Pt/C assemblage from the water-rich ink, since G' of the strained ionomer-Pt/C assemblages recovers only 1.04%, 17.1%, 20.8%, and 27.3% at 5 s, 30 s, 60 s, and 300 s, respectively. Since the water-rich ionomer-Pt/C assemblage is an attractive system, the limited structural recovery can thus be attributed to a high extent of agglomeration which certainly is not favorable for the pristine microstructure of CL. As for the ionomer-Pt/C assemblage from the IPA-rich ink, the G' recovers to 58.7%, 77.3%, 83.7%, and 96.3% at 5 s, 30 s, 60 s, and 300 s respectively, suggesting strong ability to rebuild the structural linking, which is necessary for preserving the pore structure in the pristine CL microstructure.
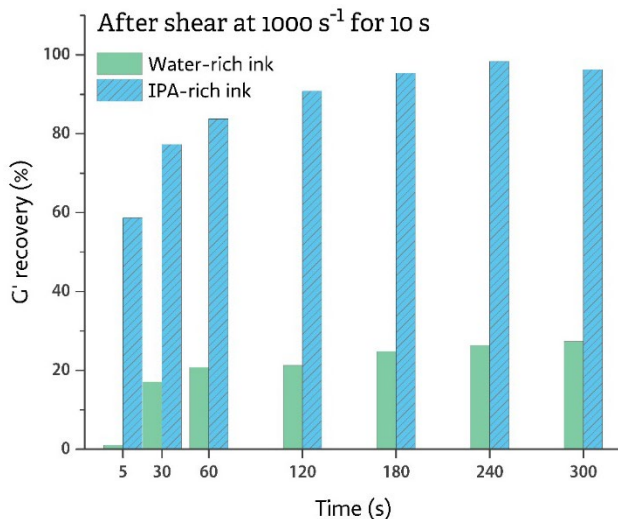
Figure 4.6. Microstructure recovery of water-rich and IPA-rich inks after the simulated shear conditions.

4.5 The source of heterogeneity of the hierarchical ionomer-Pt/C skeleton—the pristine catalyst layer microstructure

Thereafter, the solidified structures of the ionomer-Pt/C assemblages in the CL thin films are shown in Figure 4.7.

In the water-rich sample, the solidified particulate structure of ionomer-Pt/C assemblages is rather coarse and haphazardly embedded with extensive bodies of free ionomer (smooth surface) as seen in Figure 4.7a. On one hand, the strands of the network are frequently found sparse, randomly oriented, and coarsely sized, which lead to widely sized pores and agglomerates (shown in Figure 4.7c and Appendix). On the other, the embedded free ionomer pools around the particulate

network with glue-like texture and often shows ductile fracture that necks from thick bases into elongated threads (Figure 4.7e).
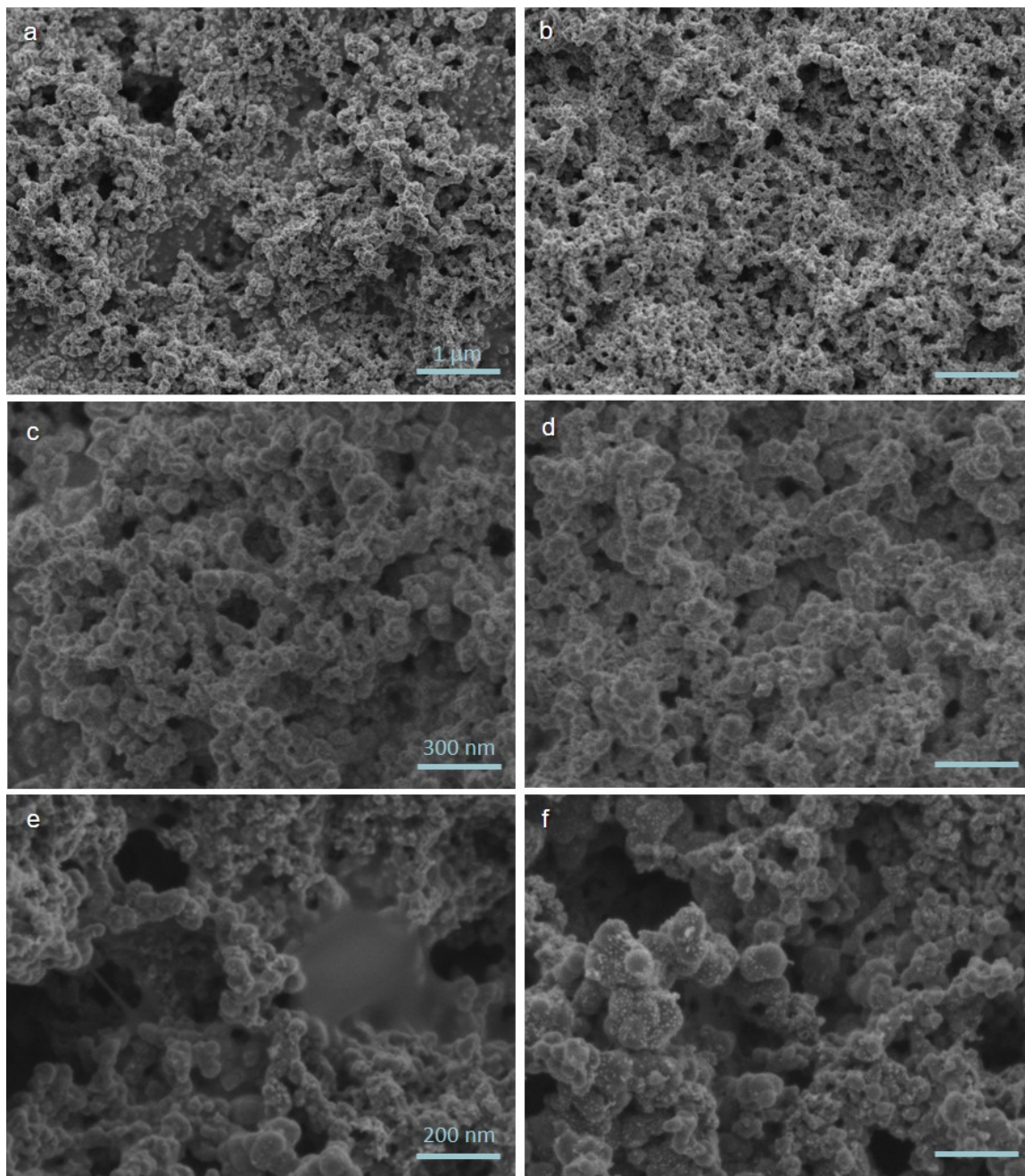
Figure 4.7. FESEM observation on (a and b) overall texture of ionomer-Pt/C particulate network, (c and d) strand structure of the network, and (e and f) ionomer aggregate morphology and fracture, in pristine CLs made from (a, c and e) water-rich and (b, d and f) IPA-rich catalyst inks. The scale bars represent 1 μm in a and b, 300 nm in c and d, and 200 nm in e and f.

In the IPA-rich sample, the particulate network has relatively fine texture with free ionomer rarely spotted as seen in Figure 4.7b. The structure of the strands tends to be chubby, nearly tetrahedral, and slightly varisized, leading to relatively narrow-sized pores and agglomerates (Figure 4.7d). In Figure 4.7f, the barely found free ionomer seems to be surrounded by the particulate structure and pulled into sheet-like form, which shows brittle type fractures that neck into flimsy strings with the base hardly seen.

The distinct morphological and fracture behavior of the free ionomer observed from the water-rich and IPA-rich pristine CLs can be attributed to corresponding gelation behaviors which are governed by the solvent composition and affinity to the ionomer chains presented in Figure 4.1. In water-rich environment, with aggregated backbones ionomer transforms from swollen clusters (due to solvated sulfonate group on side chains), condenses into precipitates, and further solidifies into hydrophobic semi-crystalline domain and hydrophilic domain phase-segregated structure that shows a glue-like texture. Whereas in IPA-rich environment, the backbone-solvated ionomer forms elliptical particles which tends to solidify into a film with more amorphous structure.[67, 91, 140] Thus, when fracture occurs the ionomers solidified from the two chemical environments exhibit different fracture behavior as the deformation starts with ionic crosslinks in amorphous domains and then the semi-crystalline domains.[141]

The observed generic characteristics of the network texture and strand structure manifesting the global and local structure characteristics can be attributed to the synergistic effect between the ionomer adsorption and the Pt/C nanoparticle clustering in the liquid phase. Based on the previous discussion on data presented in Figure 4.2 and 4.3, the growth of the intact particulate structure in the water-rich and IPA-rich system seems to follow different processes. In the water-rich system, the aggregated ionomer is adsorbed preferably at the outer surface of the Pt/C aggregates and agglomerates through carbon and induces flocculation by bridging while the Pt/C aggregates and agglomerates constantly evolving, forming coarse clusters.[74, 78, 88-89] However, the presence of the Pt in the water-rich system not only increases the surface roughness but also alters the electronegativity of the surface hampering intra-cluster aggregation and ionomer adsorption.[68, 78, 136] In the IPA-rich system, the non-aggregated ionomer can be easily absorbed on Pt/C particles though carbon forming finely densified clusters. With limited solvation, the sulfonate group on the ionomer side chain may also interact with Pt and enhance the adsorption. The enhance adsorption can cause weak entropic and steric repulsion that make the clustering of the ionomer-Pt/C

particles by corrugated locking.[142-144] The hypothesized clustering mechanisms for the water-rich system and the IPA-rich system are diffusion limited cluster aggregation, which forms varisized loose structure and slippery diffusion limited cluster aggregation, which forms locally dense elastic space-filling structure respectively.[145] In short, besides the ionomer conformation, the synergistic effect between the ionomer adsorption and the Pt/C nanoparticle clustering gives rise to the intact structure of the ionomer-Pt/C assemblage, which later deforms and eventually solidifies into the particulate network of the pristine CL.

Remarkably, the structural transformation to the pristine CL from intact ionomer-Pt/C assemblage in the catalyst ink is unneglectably affected by shear, especially to the water-rich system. The contrasting shear responses of the water-rich and IPA-rich ionomer-Pt/C assemblages, shown in Figure 4.5 and 4.6, are direct results of their flow properties, which are governed by the cluster structure and the intra-cluster forces within the system. As the Herschel-Bulkley model fitting results depicted, the water-rich ionomer-Pt/C assemblage exhibits relatively weak interparticle force (or neighborhood hinderance), ease of breakage, and limited structural connectivity. These structural characteristics indicates a structure of coarsely densified and loosely connected clusters surrounded by potentially large pools of free liquid. As for the IPA-rich, the ionomer-Pt/C assemblage shows relatively strong interparticle force (about four-fold), more ease of breakage, and relatively high extent of structural connectivity (nearly double). These characteristics correspond to a structure of finely densified and highly flocculated clusters surrounded by small pools of bounded liquid. These speculated ionomer-Pt/C assemblage structures can be verified by the texture of the catalyst ink shown in Appendix. Also, from earlier discussion, the intra-cluster force in the water-rich and the IPA-rich system is attractive and repulsive, respectively. Therefore, when subjected to the simulated high shear, the water-rich ionomer-Pt/C assemblage exhibits drastic loss of the structural connectivity and struggles to rebuild, whereas the IPA-rich ionomer-Pt/C assemblage loses little structural connectivity and regains quickly. Note that this result was observed in the power law regime beyond the yielding regime, where the high shear produces strong hydrodynamic force field, promoting particle motion and interparticle collision, which leads to disintegration of large clusters and integration of small particles respectively at the same time.[90, 133] Due to the difference in the structure and internal force of the ionomer-Pt/C assemblage, high shear can lead to distinct restructuring to the water-rich and the IPA-rich systems. In the attractive water-rich system, shear of 1000 1/s can lead to breakage and interpenetration of loosely connected large ionomer-Pt/C clusters, alignment and collision of the small particles, and extensive redistribution and local adsorption of the non-adsorbed

ionomer, rendering a highly heterogenous structure. While in the repulsive IPA-rich system, shear of 1000 1/s can lead to disintegration and interpenetration of highly flocculated fine ionomer-Pt/C clusters, alignment and relocking of small structures, and also extensive redistribution and local adsorption of the non-adsorbed ionomer, rendering a seemingly homogenous structure. These structures then solidify into the microstructure of the pristine CLs, with certain extend of shrinkage and potential collapse of the network during the drying process.[76, 85, 115] The abovementioned structure formation processes for the water-rich and IPA-rich systems are illustrated in Figure 4.8.
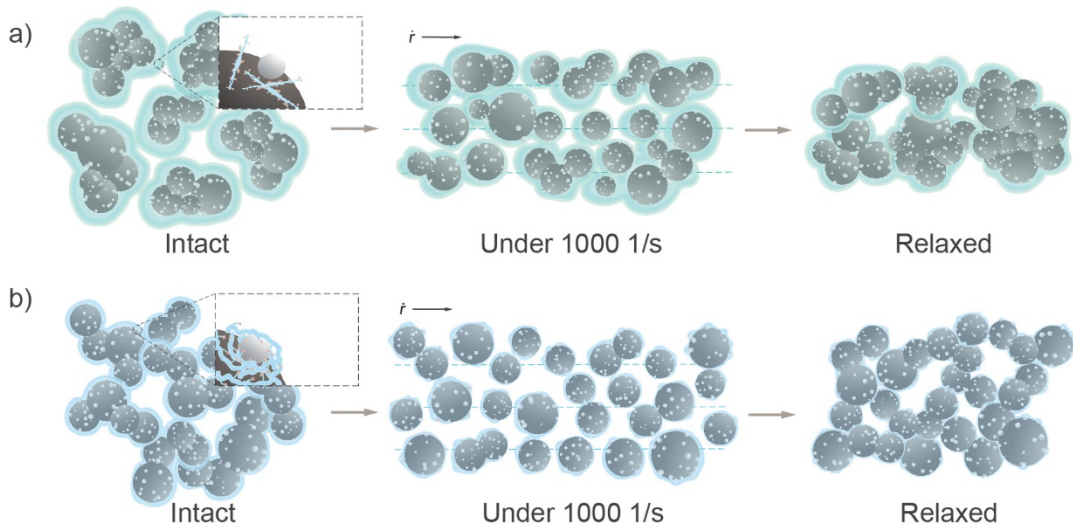
Figure 4.8. Schematic diagram of high shear-induced restructuring of ionomer-Pt/C assemblages in the water-rich and the IPA-rich catalyst inks.

The distinct spatial distributions of the free ionomer shown in Figure 4.7a and b indicate different equilibriums of ionomer adsorption on Pt/C nanoparticles in the water-rich and IPA-rich environment, which is supported by the data in Figure 4.2. With the same ionomer content, the difference in ionomer adsorption equilibrium can be attributed to not only the ionomer conformation and interaction with Pt/C nanoparticle surfaces, but more importantly the relative rate between the adsorption of the ionomer and the Pt/C nanoparticle growth in the liquid environment.[133] In the water-rich environment, the backbone-aggregated morphology of the ionomer can hamper rapid and massive adsorption on the Pt/C particles, disadvantaging the competition with particle growth. This can lead to low adsorption equilibrium and low ionomer usage, leaving the non-adsorbed especially non-associated ionomer randomly suspending around ionomer-Pt/C

assemblage in the system. After experiencing shear and gelation, the suspended ionomer eventually solidifies randomly embedded free ionomer in the pristine CL. In the IPA-rich case, non-aggregated ionomer can be adsorbed rapidly and massively before the Pt/C particles grow extensively, which leads to high adsorption equilibrium and high usage of the ionomer with little free ionomer being left to suspend around. With the aid of high shear, free ionomer can be absorbed rapidly once the non-adsorbed Pt/C surface exposes, leaving less free ionomer suspending in the system which is hardly seen in the solidified structure.

4.6 The formation of the transport-related structural heterogeneity

It is worthy to point out that the ionomer conformation and interaction with Pt/C nanoparticle surfaces also greatly affect the local morphology of the ionomer adjacent to catalyst surface and the spatial coverage on Pt/C nanoparticles. Besides solid surface condition, the interfacial distribution of adsorbed ionomer, associated ionomer, and free ionomer confined during solidification to the associated ionomer together set the tone for the spatial coverage and local morphology of ionomer nanofilm on Pt/C particles [25, 35, 97]. Due to the dual property of the ionomer chains, the hydrophobic and hydrophilic domain-segregated morphology of this ionomer-rich phase tend to constantly evolve around Pt/C surfaces through solidification.[93] For the adsorbed water-rich ionomer, the aggregated backbones and the highly solvated sulfonate groups on the side chain can solidify and form crystallites and ionic domains, which are eventually parallel to and in contact with the catalyst surface respectively.[113, 146] Moreover, the aggregation of the backbone can facilitate non-uniform spatial distribution of the ionomer contributing to more heterogeneity in the ionomer phase. As for the adsorbed IPA-rich ionomer, non-aggregated backbones and weakly solvated sulfonate groups on the side chain tend to solidify and form more amorphous structure, which favors uniform surface coverage. Yet, due to strong adsorption on Pt/C nanoparticles, thickness of the ionomer phase on the catalyst surface can be relatively large compared to the water-rich scenario with the same ionomer concentration.

Consequently, the local structural characteristics of the ionomer phase around the catalyst surface and the global structural characteristics of the ionomer-Pt/C assemblage together governs the transport pathways for not only oxygen but also proton, electron, and water in the CL. Despite the seemingly unpreferable local and global structural characteristics, the solidified water-rich ionomer-Pt/C assemblage has been reported under both dry and wet operating conditions to show relatively low resistance for both charge and mass transport, compared to the IPA-rich one with the same ionomer content.[42, 147] This observed phenomenon suggests

the complexity lying in the structure-property relationship of the CLs, which warrants further study.

CHAPTER 5

STRUCTURE AND TRANSPORT RELATIONSHIP OF THE CATALYST LAYER

In the previous chapter, the hierarchical structure of the ionomer-Pt/C assemblage was found to be governed by the chemical nature of the liquid medium used in the catalyst ink. Considering the environmental impact, the water-rich system was employed in this chapter to establish the structure-transport relationship of the CL. Since the catalyst ink used in this research is a three-component system of solvent, ionomer, and Pt/C nanoparticles, the intertwinement between these components will be focused.

In the CL, ionomer is a critical component. It serves as both the binder for the inorganic nanoparticles and the ionic pathway for protons. Tuning the ionomer weight content in the CL is always a fine art of work, as it affects gas permeability, catalytic activity, ionic conductivity, and pore property. Ionomer content in the CL is often regulated for optimal performance of the CLs. Recent studies revealed that the transport issues of the low-loading and non-PGM CLs arise from non-uniform spatial distribution and thickness of ionomer covering catalyst surface. Understanding these structural characteristics from a fundamental level with respect to the fabrication process can provide strategical insights for the CL design.

In the catalyst ink, the design factor corresponding to the ionomer content in the CL is ionomer-to-carbon (I/C) weight ratio, which fundamentally tunes the ionomer concentration in the system. The carbon concentration is controlled by another formulation parameter, solid content, which is the weight percentage of total ink solids including both the inorganic nanoparticles and the ionomer, regulating total particle concentration or interparticle distance. In the ink formulation process, these two factors, I/C ratio and solid content are commonly involved. In particular, I/C ratio has been intensively studied and found to strongly impact on the transport resistance by affecting ionomer thin-film morphology and the agglomerate size in the CL.[148-151] Solid content, which controls the carbon concentration, on the other hand, is often overlooked. Based on the literature, particle concentration has a dominant impact on the packing of the particulate structure.[80, 87, 152] This implies that by regulating carbon concentration solid content can play a non-trivial role in the formation of the structure of the ionomer-Pt/C assemblage. In other words, by controlling ionomer concentration and carbon concentration, I/C ratio and solid content are expected to have an interdependent

effect on the formation of the ionomer-Pt/C assemblage and the structural translation to CLs, which can be investigated by the approach from the previous chapter to provide a fundamental understanding on the formation of ionomer distribution in the CL. It is also rational to hypothesize that I/C ratio and SC have a compound effect on the formation of the CL microstructure and consequently the transport properties.

Herein, this chapter attempts to 1) elucidate the roles of the I/C ratio and the solid content in the formation of the CL microstructure and 2) demonstrate the compound effect of the I/C ratio and the solid content on the mass transport, in particular the oxygen transport. Since ionomer/carbon ratio and solid content are associated factors, both factors can be studied simultaneously via a two factor-three level fractional design of experiment. The goal is to provide strategic insights for designing and optimizing CL based on structure-process-property relationship.

Table 5.1. Sample code and control parameters.

Sample	I/C ratio	Solid content (%)	φ_c (%)	φ_i (%)
IC05SC06	0.5	6.25	1.5	0.96
IC05SC20	0.5	20.0	5.1	3.95
IC15SC06	1.5	6.25	1.1	1.96
IC15SC20	1.5	20.0	3.6	6.84
IC10SC13	1.0	13.5	2.8	3.60

The catalyst inks were made of Pt/C (40 wt.% Pt on Vulcan, JM HiSPEC 4000), PFSA ionomer (20 wt.% Nafion, Dupont D2020), and water-isopropyl alcohol (IPA, HPLC grade, Sigma Aldrich) binary solvent with IPA volume fraction of 0.25. The I/C ratio and solid content were controlled ranging from 0.5 to 1.5 and from 6% to 20%, respectively. The resulting ionomer-Pt/C assemblages are labeled based on their design parameters as shown in Table 5.1. Considering the physisorption of ionomer at carbon surface in aqueous environments,[78] the volume fraction of the carbon (φ_c) and the ionomer (φ_i) are also presented in Table 5.1 for reference. All the samples were prepared by a high-shear mixer (AR-100, Thinky USA) operating at 2000 rpm for 4 minutes with 7 zirconia beads (dia. 5 mm) in a 12 mL ointment container loaded on an adaptor 100AD-NAN-U. The

particle size distribution and rheological measurement are the same as the previous chapter. In addition to field emission SEM, the CLs were also assembled into MEAs for electrochemical measurements following the protocol listed in Table 3.1.

5.1 The local and global structural characteristics of intact ionomer-Pt/C assemblages

To elucidate the roles of I/C ratio and solid content in the formation of the CL microstructure, the local and global structural characteristics of the ionomer-Pt/C assemblage with respect to the formation process of the CL microstructure was investigated and presented in the following.
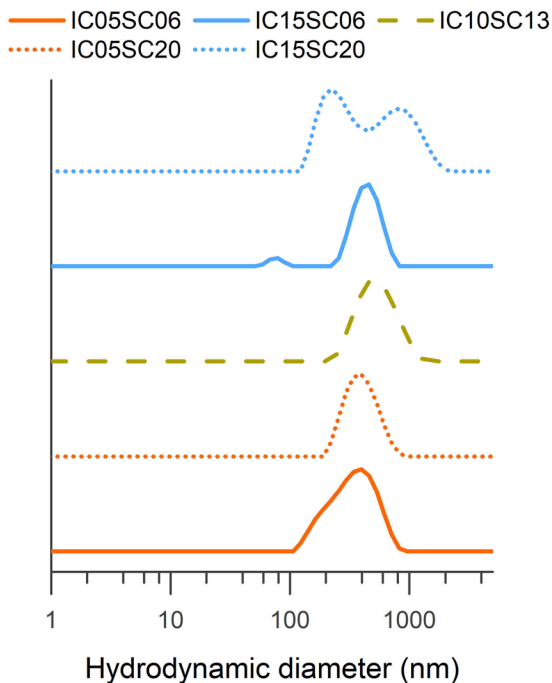
Figure 5.1. Hydrodynamic diameter of particles from dilute dispersions of corresponding catalyst inks of various I/C ratios and solid contents.

The size distributions of the particles from various catalyst inks were used for understanding the ionomer-Pt/C interaction and the resulting local structure of the ionomer-Pt/C assemblage. The data shown in Figure 5.1 demonstrate the complexity of the ionomer-Pt/C interaction caused by I/C ratio and solid content. As discussed in previous chapter, the local structure of the self-associated ionomer-Pt/C assemblage is a concurrent result of ionomer aggregation, ionomer adsorption,

and particle aggregation, which can be inferred from the size distribution of particles in a dilute system. From previous chapter, it was clear that the broaden peak of size distribution snapshots ongoing reversible interparticle association due to ionomer bridging effect. At high I/C ratio, this phenomenon becomes more pronouncing as IC15SC06 and IC15SC15 both exhibit bimodal size distribution, which indicates strong aggregation and adsorption of abundant amount of the ionomer. For the systems with low I/C ratio, ionomer aggregation seems to give in to the adsorption on Pt/C aggregates rendering unimodal size distribution with relatively broad peak. On the other hand, the role of the solid content in determining the size distribution is not straightforward. As shown in Table 5.1, solid content has a closer tie to the carbon volume fraction at low I/C ratio (0.5), but more related to the ionomer volume fraction when I/C ratio is relatively high (1.5). As shown in Figure 5.1, increasing solid content at a low ionomer concentration leads to narrower unimodal size distribution of the ionomer-Pt/C assemblage without evident peak shift due to enhanced ionomer adsorption. However, in the case of high ionomer concentration, increasing solid content not only causes broad bimodal size distribution, but also significant shift of the peaks to larger particle sizes, suggesting strong clustering of the particles.
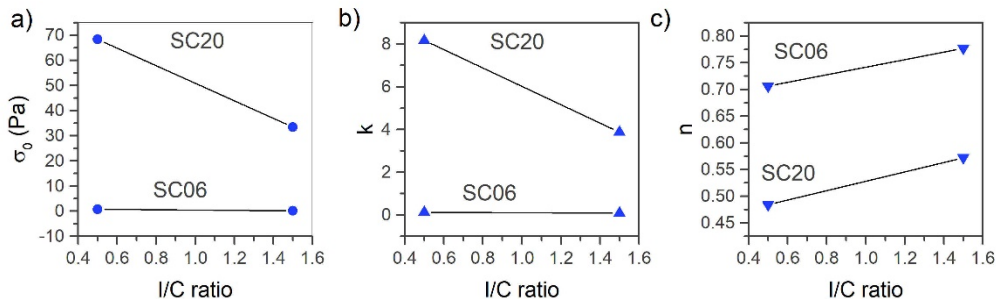
Figure 5.2. Herschel-Bulkley parameters of the ionomer-Pt/C assemblages in catalyst inks of various I/C ratios and solid contents: (a) apparent yield stress, σ_0 (Pa), (b) consistency index, k, and (c) flow index, n.

According to the results from the previous chapter, the self-associated water-rich ionomer-Pt/C assemblage, resulted from the adsorbed ionomer at the outer surface of the Pt/C aggregates, is prone to form a coarsely densified structure potentially via diffusion limited cluster aggregation mechanism. Therefore, the ionomer spatial distribution and the packing of the particulate structure of each sample can differ drastically with various I/C ratios and solid contents. The

detailed local and global structure of these ionomer-Pt/C assemblages formed by each combination of the I/C ratio and solid content are discussed in the later part of this section.

As for the intact global structure of the ionomer-Pt/C assemblages in the catalyst inks, the structural characteristics in terms of flow properties were depicted by Heschel-Bulkley (HB) parameters, which include apparent yield stress, σ_0 (Pa), consistency index, k, and flow index, n. Note that n describes the extent of shear-thinning nature of the sample when less than 1. The smaller value, the more shear-thinning. These empirical parameters quantitatively describes the flow properties as the results of the internal structure of the complex fluid. Therefore, in this chapter, they are used to describe the internal structure of the ionomer-Pt/C assemblages in the catalyst inks from three different aspects: 1) σ_0 for the inter-cluster forces in the Brownian regime, 2) k for the extent of structural crosslinking, and 3) n for the intra-cluster strength of the ionomer-Pt/C assemblage in the catalyst ink. The effects of I/C ratio and solid content on the HB parameters are presented in Figure 5.2.

As shown in Figure 5.2a, the solid content and I/C ratio affects σ_0 interdependently. σ_0 is sensitive to the solid content over I/C ratio. In particular, at low solid content I/C ratio show very limited effect on σ_0. Such effect of the solid content also manifests in the structural crosslinking as shown in Figure 5.2b. These results indicate the dominant contribution of Pt/C aggregates to the intra-cluster strength and the structure crosslinking of the intact global structure. Notably, at high solid content both σ_0 and k values decrease with increasing I/C ratio, indicating severe structural mediation by ionomer aggregates in between the cluster surfaces as φ_i is nearly twice φ_c (Table 5.1). However, the effects of solid content and I/C ratio on n are much more distinct as the n values in Figure 5.2c are positively proportional to the I/C ratio, but negatively proportional to the solid content. The data show in Figure 5.2c suggest that the intra-cluster force increases with increasing I/C ratio and/or decreasing solid content, profiling the extent of aggregated ionomer mixing with Pt/C aggregates in the clusters.

The structural characteristics of the ionomer-Pt/C assemblage are essential to the electrochemical and transport properties of the CL, since the structure of the ionomer-Pt/C assemblage is the cornerstone of the particulate structure of the CL. Specifically, the morphology and connectivity of the Pt/C phase and the morphology and the spatial distribution of the ionomer phase together affect the spatial distribution of the electrochemical reaction sites and the connectivity of pathways for the reactant and product transport. As the water-rich systems, the ionomer-Pt/C assemblages studied in this chapter are attractive systems due to

ionomer bridging effect at the outer surfaces and tend to form coarsely densified and loosely connected clusters. Based on the hydrodynamic size distribution and HB parameters, the local and global intact structure of these ionomer-Pt/C assemblages are summarized as follows.

For IC05SC06, the low concentrations of the ionomer and the Pt/C particles does not promote high extent of ionomer aggregation and Pt/C aggregation. The broad peak shown in Figure 5.1 indicates the dynamics of reversible particle self-association, which suggest strong bridging effect of the ionomer aggregates at the carbon surface of the Pt/C aggregates.[71, 123] The local structure thus is primarily the result of strong ionomer adsorption (due to high rate) at the outer carbonaceous surface of the Pt/C aggregates, which leads to a local structure of varisized fine Pt/C particles with backbone-aggregated ionomer highly infiltrated. The HB parameters of IC05SC06 suggest low inter-cluster force (or neighborhood hinderance), limited structural crosslinking, and high intra-cluster strength of the global intact structure, resembling a highly fractal, weakly connected, and highly ionomer-infiltrated particulate structure.

In the case of IC05SC20, due to the increasing φ_i and φ_c, locally ionomer adsorption and Pt/C aggregation are highly promoted as $\varphi_c > \varphi_i$. This situation can lead to rapid adsorption of a thin layer of ionomer at the surfaces of the clustering Pt/C aggregates, resulting in a narrow size distribution as shown in Figure 5.1. Meanwhile, the HB parameter verifies that the global intact structure of IC05SC20 owns the highest inter-cluster force, highest extent of structural crosslinking, and lowest intra-cluster strength, indicating a highly rigid and massively connected particulate network.

As for IC15SC06, the fact that $\varphi_i > \varphi_c$ favors ionomer aggregation and adsorption at local scale. Consequently, separate bodies of ionomer in the system can be expected, which is indicated by the tiny peak (<100 nm) in Figure 5.1. On the other hand, with the small φ_c, Pt/C aggregation can be mediated by the aggregated ionomer in addition to ionomer adsorption, leading to the formation of fine clusters with free bodies of ionomer around. According to the HB parameters, the global structure of IC15SC06 shows low inter-cluster force, limited structural crosslinking, and the highest intra-cluster strength, suggesting a soft particulate structure highly mediated by ionomer.

When it comes to IC15SC20, both φ_c and φ_i increase and φ_i is nearly twice of φ_c, in which case although ionomer aggregation, ionomer adsorption, and Pt/C aggregation are encouraged at the same time, ionomer aggregation and adsorption are expected to be more aggressive, mediating the Pt/C aggregates. Inevitably, as described by the broad joint bimodal size distribution in Figure 5.1, two scales of

clusters with peak sizes of about 100 nm and 1000 nm, respectively, exist and congregate at the same time. Such complex aggregation phenomena can lead to a highly heterogenous local structure with large Pt/C aggregates and phase-separated ionomer aggregates. The HB parameters suggesting moderate inter-cluster force and structural crosslinking, and relatively low intra-cluster strength indicate a global structure of densified cluster with thick layer of adsorbed ionomer and free bodies of ionomer.

5.2 The shear-induced restructuring of the ionomer-Pt/C assemblages and the pristine catalyst layers

The previously mentioned morphological features of the intact ionomer-Pt/C assemblages provide insights into the hierarchical structure of the pristine CL. Nevertheless, the functional ionomer-Pt/C assemblages are the ones that go through restructuring due to high shear process, rather than the intact ones mentioned above. The electrochemical and transport properties of the restructured ionomer-Pt/C assemblages are determined by the restructured morphology of the Pt/C phase and the ionomer phase. Therefore, in addition to the flow properties, the shear-induced behavior of the global structure of the ionomer-Pt/C assemblage in the catalyst inks were also measured to understand the structure change induced by the simulated shear application. Since the structure of all the samples were characterized to be elastic space-filling gels (constant elastic modulus, G'), only the plateau G' values and shear-induced percentage recovery of G' are focused and presented in Figure 5.3.[153]

As shown in Figure 5.3a, the G' values of the networks depend greatly on the solid content, indicating the primary contribution from the rigid Pt/C particles. It is also clear that increasing I/C ratio only softens the networks irrespective of the solid content, since the G' value decreases with increasing I/C ratio. Note that the G' value of the intact particulate network in the catalyst ink can change drastically due to shear process.

Figure 5.3b presents the percentage recovery of G' after a simulated shear process of 1000 1/s for 10 s. The percentage recovery of G' seems to be interdependently affected by I/C ratio and solid content. In particular, the samples with high solid content exhibit structural resilience to the simulated shear process, which can be attributed to the rigid and high connected particulate structure. However, a high I/C ratio at low solid content (IC15SC06) provides limited structural resilience to the simulated shear process, potentially due to high extent of ionomer infiltration in the system.
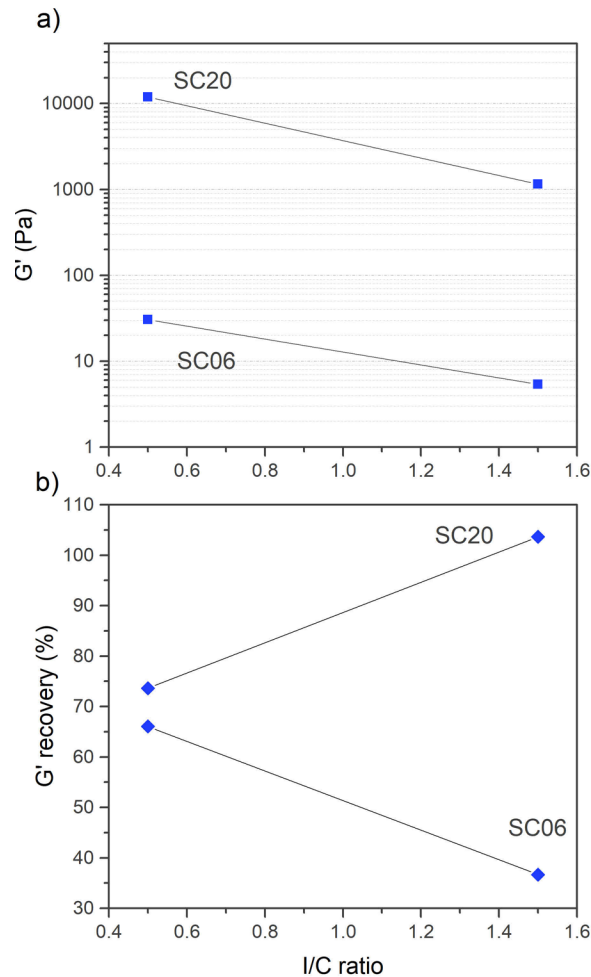
Figure 5.3. (a) Elastic modulus, *G'*, of the intact global structure of the ionomer-Pt/C assemblage in the catalyst inks of various I/C ratios and solid contents. (b) Percentage recovery of *G'* of the sample structure from applied shear of 1000 1/s for 10 s as a simulated coating process.

Specifically, as the data in Figure 5.3b suggested, most of the ionomer-Pt/C assemblages in the catalyst ink recovers less than 80%, meaning a considerable loss of the percolating structure. After being subjected to the simulated shear condition of 1000 1/s for 10 s, only IC15SC20 is free from loss of elastic connectivity while the others have lost certain extent of the elastic response after the restructuring. The loss of the elasticity of the ionomer-Pt/C assemblage in the catalyst inks can be attributed to spatially redistribution of the ionomer when subjected to high
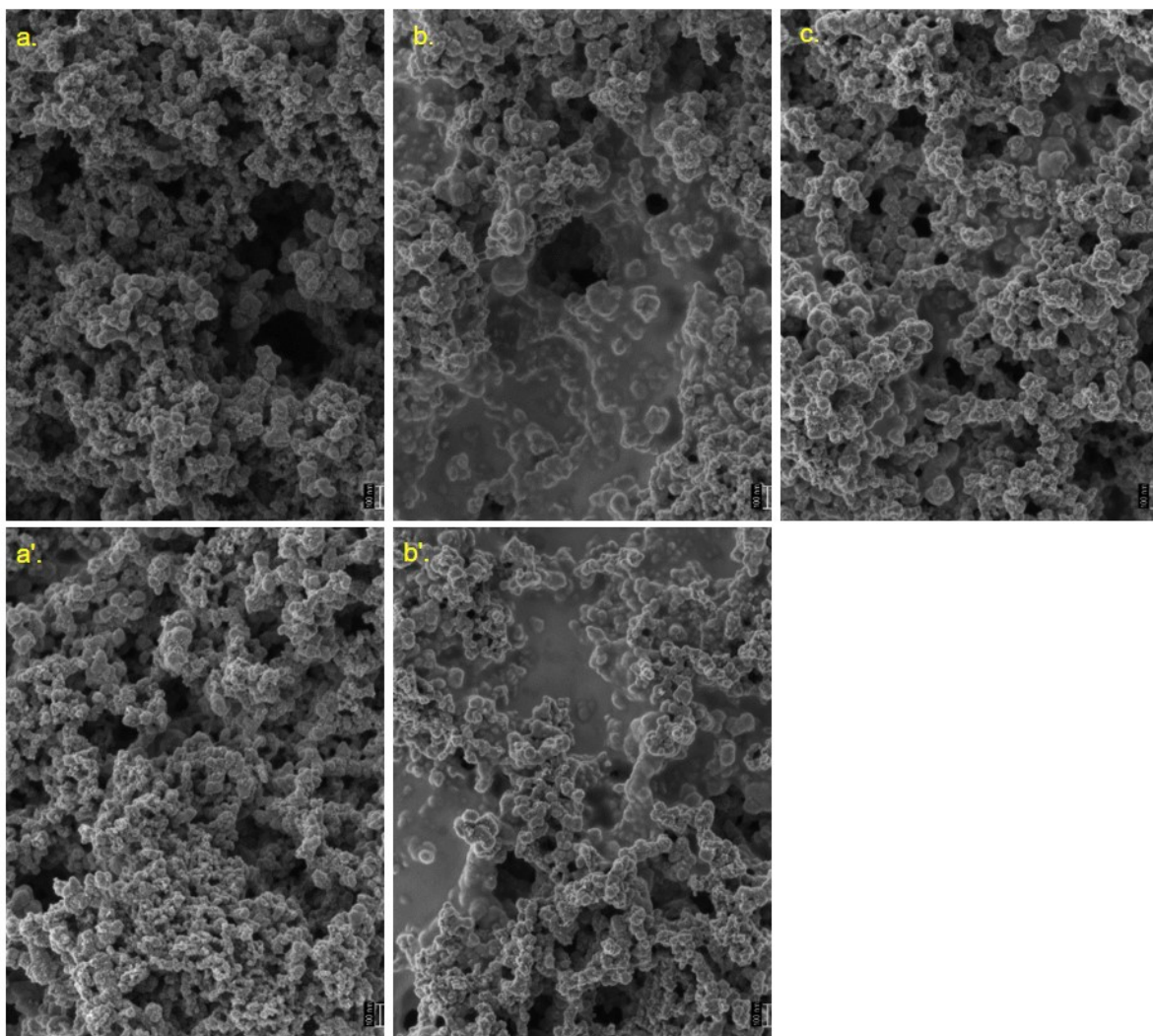
Figure 5.4. FESEM images of the pristine catalyst layers of various I/C ratios and solid contents: a. IC05SC06; a'. IC05SC20; b. IC15SC06; b'. IC15SC20; c. IC10SC13. The scale bars represent 100 nm.

shear. Due to the attractive nature of the assemblages, it is rational that the restructuring favors coalescence due to ionomer aggregation and adsorption, which can lead to interpenetrated clusters or densified agglomerates.[75, 153] This explains the distinct percentage recovery of G' for IC15SC06 and IC15SC20, as the adsorption equilibrium of ionomer on the carbon surface depends on both the surface area and surface roughness.[68-69] In the case of IC15SC20, the recovery overshoot is attributed to depletion repulsion caused by redundant ionomer in the system. Based on present explanation, it seems that the global particulate structure has a lower bound on the connectivity below which restructuring of local structure

into a more compact one is inevitable. This speculation agrees with the analysis in the literature, where the lower bound in terms of fractal dimension was found to be 2.4 for fully developed clusters.[154] In other words, for the attractive ionomer-Pt/C system in this study, high shear promotes interpenetration of clusters mainly as a result of ionomer redistribution, adsorption, and aggregation. The electrochemical and transport properties of the CL would highly depend on the phase-segregated morphology of the restructured ionomer-Pt/C particulate structure.

Figure 5.4 presents the FESEM images of the pristine CLs. Apart from the evident bodies of free ionomer at high I/C ratio shown in Figure 5.4b and 4b', it is clear that the texture of the particulate network becomes densified with more structural crosslinking as the solid content increases. The observed structural densification caused by high solid content agrees with the simulation in the reference that for an attractive system high volume fraction of the solid particles produces more spatially homogenous gels.[152] The observed morphological characteristics of the CLs agree with previous discussion on the global structural characteristics of the ionomer-Pt/C assemblages in the catalyst inks.

5.3 Transport properties of the catalyst layers

A detailed portrayal of the roles of I/C ratio and solid content on the transport properties extracted from the fuel cell diagnosis measurements are presented in Figure 5.5. To avoid the complexity caused by the relative humidity (RH), ECSA and R_{H^+} were measured under wet condition while $R_{O_2}^{p,d}$ and $R_{O_2}^{p,i}$ were measured under dry condition. As shown in Figure 5.5a, ECSA is more of dependence on I/C ratio but becomes sensitive to solid content when I/C ratio is lower than 0.6. This observation is rather important because it suggest that more reaction sites can be achieved by using low I/C ratio with high solid content. However, to minimize R_{H^+} a moderate I/C ratio and solid content no greater than 12% would be preferred as suggested in Figure 5.5b, where shows that R_{H^+} is surprisingly sensitive to solid content. More surprisingly, as shown in Figure 5.5c and 5d, both $R_{O_2}^{p,d}$ and $R_{O_2}^{p,i}$ depend on not only I/C ratio but also solid content. It is well understood that high I/C ratio tends to result in surplus ionomer embedding in the CL microstructure hampering oxygen transport.[91] However, the interdependent roles of solid content and I/C ratio in affecting oxygen transport to our best knowledge is first time revealed. The correlations between the desirable transport properties and the structural characteristics of the ionomer-Pt/C assemblage are discussed in the following.
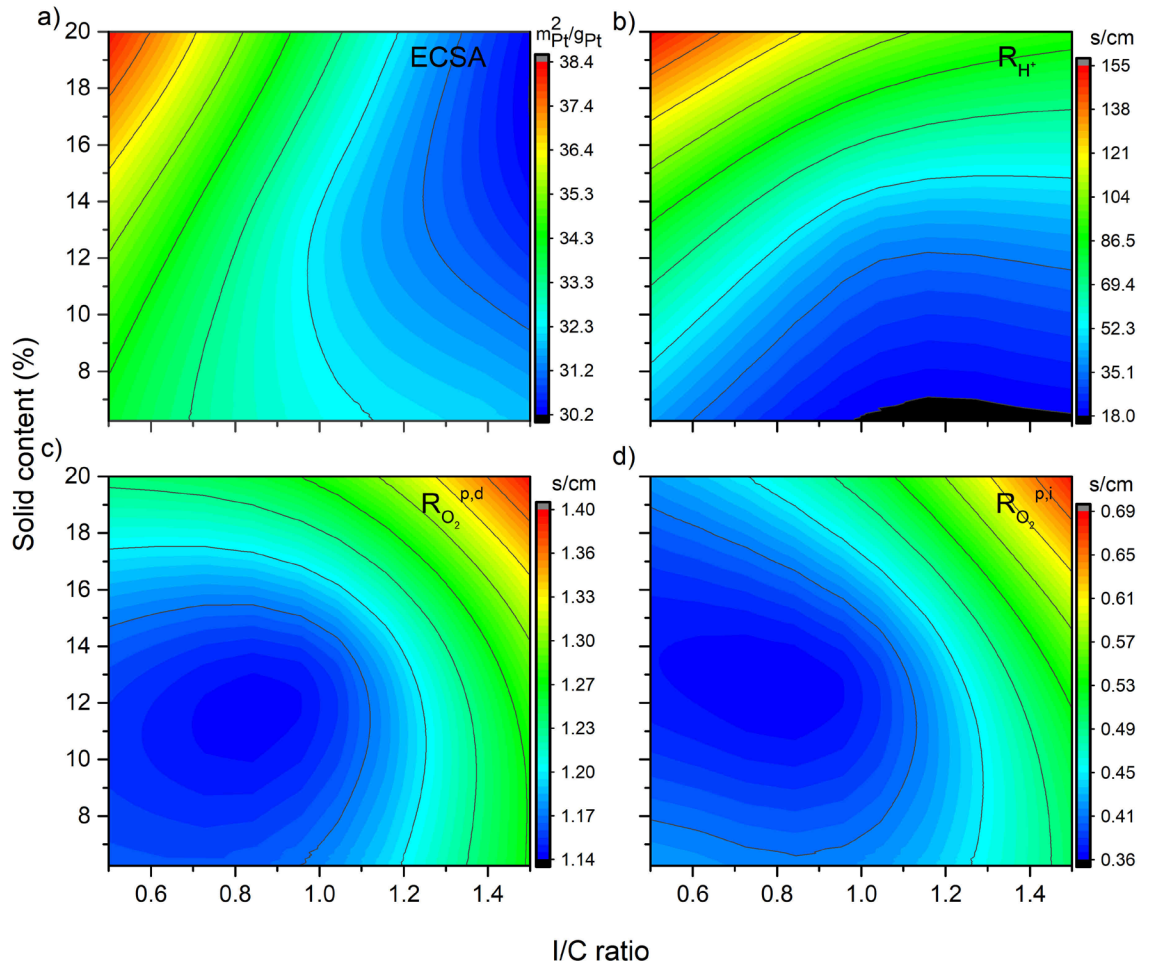
Figure 5.5. Contour plots of (a) electrochemically active surface area, ECSA, (b) proton transport resistance, R_{H^+}, (c) pressure-dependent oxygen transport resistance, $R_{O_2}^{p,d}$, which in this study excludes the transport resistance in the flow channels and corresponds to the value measured at 300 kPa, and (d) pressure-independent oxygen transport resistance, $R_{O_2}^{p,i}$, as functions of both I/C ratio and solid content.

The ECSA profile based on the measured data associates directly with the particulate structures of the CLs. Since the same amount of the Pt catalyst is used in the measured CLs, the variation of the ECSA value can only attributed to the difference of accessible ionomer|Pt interface in the ionomer-Pt/C skeleton of the

51

CLs. According to Figure 5.5 and previous discussion on the ionomer-Pt/C assemblages in the catalyst inks, the desirable high value of ECSA can be achieved by a structure with more particulate connectivity with low ionomer content. However, the proton transport favors high ionomer content for ionic rather than particulate connectivity. Such a dilemma highlights the nature of heterogenous catalysis and the complexity of corresponding multiphase transport phenomena.

As for oxygen transport, both $R_{O_2}^{p,d}$ and $R_{O_2}^{p,i}$ reach minima where the solid content and I/C ratio are moderate. $R_{O_2}^{p,d}$ is the resistance related to oxygen diffusion in the bulk regime, where Fickian diffusion dominates in certain pores, of which the mean pore diameter is larger than the mean free path of the oxygen molecules (38.46-39.58 nm, 70-80°C, 300 kPa). The ionomer-Pt/C assemblage in a catalyst ink provides minimal values of $R_{O_2}^{p,d}$ featuring combined characteristics of IC05SC06 and IC10SC13, including low inter-cluster force, moderate structure crosslinking, low intra-cluster strength, and relatively high rigidity. Namely, the oxygen diffusion in bulk regime favors percolating pores (dia. $>>$ 40 nm) formed by highly connected and mechanically stable particulate structure.

As for $R_{O_2}^{p,i}$, it is the resistance associated to 1) oxygen diffusion in the small pores where Knudsen diffusion dominates and 2) oxygen diffusion through ionomer and/or water vapor. As mentioned earlier, $R_{O_2}^{p,i}$ is sensitive to the geometrical details of the particulate structure. On one hand, oxygen self-diffusion in the Knudsen regime can be significantly hindered by the tortuosity and roughness of the pathways. On the other, the resistance caused by oxygen permeation through ionomer is greatly affected by the spatial distribution of the ionomer phase in the particulate structure. Therefore, the non-pressure driven oxygen transport would favor the particulate structures with high connectivity (small fractal dimension and long strands) and limited ionomer presence. The ionomer-Pt/C structure in the catalyst ink with low inter-cluster force, high extent of structural crosslinking, low intra-cluster strength, and high rigidity would be preferred.

5.4 Fuel cell performance of the catalyst layers

It is known that the presence of liquid water has complex effects on the mass transport in the CL. Experimentally, the presence of liquid water can be controlled by regulating the RH and the operating temperature. Polarization curves measured under water condensation-free or dry condition and water condensation-promoting or wet condition are referred as dry polarization curves and wet polarization curves, respectively. RH has been found to influence the proton transport, oxygen transport, and the ECSA.[110, 155-156] Hence, the effect of I/C ratio and solid content on both

the dry and the wet polarization curves are shown in Figure 5.6 and 5.7, respectively.
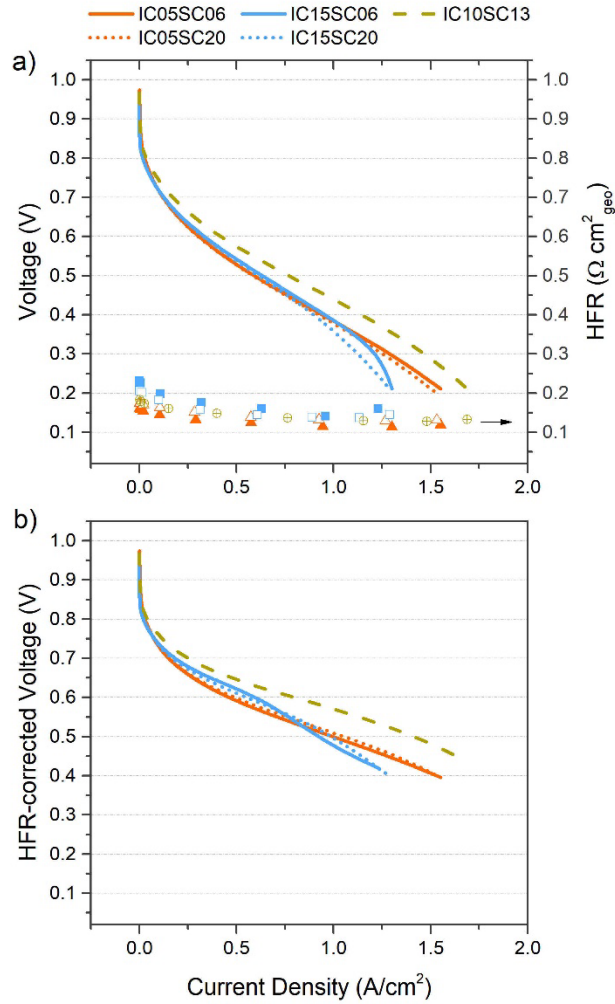
Figure 5.6. (a) Uncorrected H_2/air dry polarization curves of MEAs with various cathodic catalyst layers and corresponding high frequency resistance (HFR). (b) HFR-corrected H_2/air dry polarization curves.

Under dry condition, as shown in Figure 5.6a, the polarization curves in the mass transport regime, where the current density is larger than 1.25 A/cm², shows a predominant nonlinear dependency on I/C ratio. This dependency can be attributed to the roles of the ionomer in hampering oxygen transport and masking reaction sites. With HFR corrected, Figure 5.6b further shows the predominant influence of I/C ratio on the dry polarization curves, not only the mass transport

but also the proton transport. Especially for the samples of high I/C ratio, the onset of mass transport starts at a surprisingly low current density of 0.7 A/cm^2. Under such a dry condition, the slight effect of solid content on the mass transport is almost negligible.
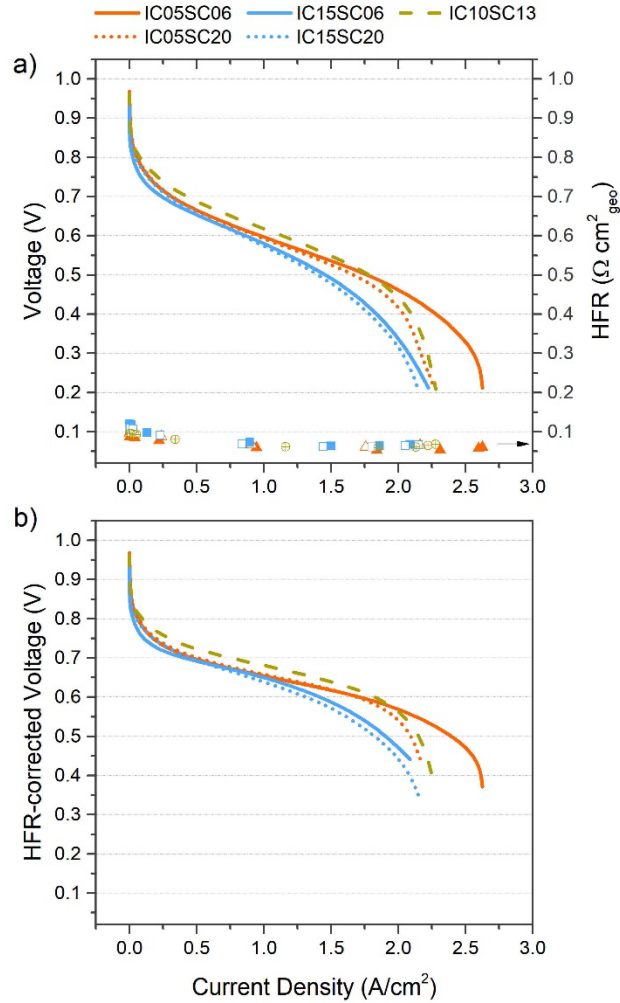
Figure 5.7. (a) Uncorrected H$_2$/air wet polarization curves of MEAs with various cathodic catalyst layers and corresponding high frequency resistance (HFR). (b) HFR-corrected H$_2$/air wet polarization curves.

Interestingly, under wet condition (Figure 5.7a), the onset of mass transport shifts to a larger current density about 2 A/cm^2; the I/C ratio-dependency of the mass transport remains dominant; however, an evident influence of the solid content appears in the samples of low I/C ratio; also, low solid content seems to

54

promote mass transport. The mass transport is most promoted by a combination of low solid content (6.25%) and low I/C ratio (0.5). These observations suggest a compound effect of the I/C ratio and solid content on mass transport under wet condition. HFR-corrected wet polarization curves in Figure 5.7b show no drastic change in the mass transport regime. Notably, in the activation regime between 0 and 0.25 A/cm^2 high solid content seems to play a positive role.

The results presented in Figure 5.5 and Figure 5.7 certainly verify the RH dependence of the transport phenomena. Clearly, under dry condition, proton transport seems to be more critical to the cell performance than oxygen transport. Indeed, under dry condition proton transport in the ionomer ionic channels becomes hindered as a sufficient amount of water is required for protons to effectively hop around the sulfonate groups at ionomer side chain.[157] This hindered proton transport further impedes oxygen transport. It is also surprising to observe the effect of solid content on the mass transport, which becomes more evident under wet condition.

Based on the RH dependence of the polarization curves, it is clear that particulate networks with sufficient ionic pathways and more importantly with mechanically stable and highly fractal long strands would facilitate the mass transport at high current density.

CHAPTER 6

CONCLUSIONS AND FUTURE WORK

6.1 Conclusions

The first part of the research qualitatively investigated the structural translation of ionomer-Pt/C nanoparticle assemblage into pristine CL and the origin of the heterogeneous characteristics of the hierarchical microstructure of suspension-cast CLs using water-isopropyl alcohol (IPA) as the chemical environments or fluid systems.

The structures of ionomer-Pt/C assemblages in dilute and concentrated systems depict two distinct hierarchical self-assembling processes, relying on the chemical environments. In the water-rich system, the backbone-aggregated ionomer is adsorbed limitedly and preferably at the outer surface of the Pt/C nanoparticles through carbon and induces bridging flocculation while the Pt/C nanoparticles constantly growing and evolving, resulting in a structure of coarsely densified and loosely connected ionomer-Pt/C clusters surrounded with potentially large pools of free liquid. In the IPA-rich system, the non-aggregated ionomer can be massively and easily absorbed on Pt/C particles though both carbon and catalyst forming finely densified clusters before the Pt/C particles grow extensively, leading to a structure of finely densified and highly flocculated clusters surrounded by small pools of bounded liquid. The impact of the chemical environment on the flow property of the intact structure of the ionomer-Pt/C assemblage is profound and significant as suggested by Herschel-Bulkley model fitting results. Compared to the water-rich ionomer-Pt/C assemblage, the IPA-rich showed four-time interparticle strength, nearly twice structural connectivity, and higher spreadability.

Remarkably, the shear-induced structural response of the ionomer-Pt/C assemblage in the catalyst ink discloses the unneglectable role of shear in the structural translation into the pristine CL, also depending on the chemical environments or fluid systems. When subjected to high shear, the water-rich ionomer-Pt/C assemblage with weakly attractive interparticle force (or neighborhood hinderance), ease of breakage, and limited structural connectivity, shows drastic loss of the structural connectivity, and struggles to rebuild; while the IPA-rich ionomer-Pt/C assemblage with weakly repulsive interparticle force, more ease of breakage, and relatively high extent of structural connectivity, loses little structural connectivity and rebuilds three times as fast as the water-rich system.

This strong correlation established in the structural translation of the intact ionomer-Pt/C assemblage into the pristine CL unveils that the very source of the multiscale heterogeneity in the hierarchical microstructure of CL roots in not only the affinities of the chemical environment to the ionomer and the Pt/C nanoparticles, but perhaps the most overlooked, the shear exerted on the ionomer-Pt/C assemblage during ink processing and casting. High shear can agitate and even degrade the structure of the ionomer-Pt/C assemblage, i.e. the precursor of the CL.

The revealed structural self-assembling process of ionomer-Pt/C assemblage suggests the observed heterogeneous structural phenomena in the CL microstructure are strongly related to the ionomer conformation and the competing relationship between the ionomer adsorption and the Pt/C particle growth, depending on the chemical environment or liquid system. The hypothetical growth mechanisms are diffusion limited cluster aggregation and slippery diffusion limited cluster aggregation for the water-rich and the IPA-rich ionomer-Pt/C assemblages, respectively. To improve the structural heterogeneous phenomena (including the local anisotropic morphology of ionomer adjacent to catalyst surface, the non-uniform ionomer coverage on Pt/C, the inhomogeneous spatial distribution of ionomer and pores, and the large agglomerates present in the microstructure of the CL), the ionomer conformation and adsorption, the Pt/C nanoparticle growth, and the shear all needs to be precisely controlled to produce the CL with tailored structure-functionality relationship.

Additionally, the distinct structural discrepancy between the ionomer-carbon assemblage and the ionomer-Pt/C assemblage in both water-rich and IPA-rich system suggests when using ionomer-carbon assemblage to approximate ionomer-Pt/C assemblage in both dilute and concentrated systems additional care should be taken.

The second part of the research qualitatively explored the effect of the I/C ratio and the solid content on the formation-structure-functionality relationship of the CLs. The RH-dependent polarization curves and the data of fuel cell diagnosis measurements demonstrated the compound effect of I/C ratio and solid content on the mass transport, especially on the oxygen transport. Oxygen transport resistance can be minimized by using I/C ratio of 0.6-1.0 and solid content of 9-13 wt.%. However, only minimizing oxygen transport does not guarantee improved mass transport, especially when liquid water presents. The non-destructive hydrodynamic size distribution and rheological measurements were employed to elucidate the roles of the I/C ratio and the solid content in the formation of the CL structure. By analyzing the local and global structure of ionomer-Pt/C

assemblages in the catalyst inks, I/C ratio and solid content were found to affect the competition between homoaggregation and heteroaggregation, the inter- and intra-cluster strengths, and the rigidity and connectivity of the particulate structure. Also, the simulated high shear application tends to reduce the connectivity of the particulate network and induce the densification of the clusters, unless the global structure is mechanically stable and resilient. For the attractive ionomer-Pt/C system in this part of the study, high shear promotes densification of the structure mainly as a result of ionomer redistribution, adsorption, and aggregation. In the catalyst ink, a gel structure with high extent of structure crosslinking, low inter- and intra-cluster strengths, and sufficient rigidity would produce ionomer-Pt/C assemblage with optimal electrochemical and transport properties. Despite many limitations in this work, overall, the results suggest that CLs with sufficient ionic pathways and more importantly with mechanically stable and highly fractal long particulate strands would facilitate the mass transport at high current densities.

6.2 Future work

Voltage loss at high current density due to diffusion type mass transport is related to heterogeneous microstructure of low-loading CLs.[25-27] One side, ionomer's role in agglomerate formation leads to heterogeneity in size and composition of agglomerates, which affects utilization of the catalyst and local transport condition related to pore property.[27-29, 148] On the other side, the interplay between porosity and thickness of CL also contributes to mass transport issue.[31] Understanding the transformation of colloids in the catalyst ink to the agglomerates in the CL will facilitate design of desired microstructure for low-loading CLs. Literatures have validated that tuning ionomer/catalyst interfacial design improves fuel cell performance.[25, 158]

Based on learnings from the last two studies, this study attempts to address transport issue caused by heterogeneous nature of agglomerates formed from ink colloids. Pt/C catalysts with two types of support surface geometry will be used. Size and charge of the ink colloids will be characterized by dynamic light scattering and electrophoretic light scattering. Rheological property will be investigated at the gap of coating thickness for low-loading CLs. Microstructure change of catalyst inks due to coating process will be investigated by incorporating a simulated shear condition. Field emission SEM will be used to observe the agglomerates in the CL. Thickness of the CLs will also be measured by SEM from cross-section and will be used to estimate porosity. Surface roughness will be characterized by profilometer. Contact angle will be measured to monitor surface property for water management. All CLs will be assembled into MEAs to characterize electrochemical properties. In

addition to standard polarization curve and AC impedance measurements, various fuel cell diagnostic tests will be carried out to derive properties that are related to agglomerate heterogeneity, ionomer distribution and ionomer/Pt interface and pore property. The electrochemically active surface area of the cathode will be measured via cyclic voltammetry to calculate electrode roughness factor. The local transport property at ionomer/Pt interface will be derived from limiting current measurements under both dry and wet conditions. Proton resistance related to ionomer distribution in the CL can be derived from AC impedance. Pore property for water management can be gauged by limiting current measurement under both wet and dry condition.

An improved design of experiment, a factorial mixture design will be adopted into this study. A simple manipulation of the ink colloids will be carried out by varying pH of aqueous catalyst inks.

As for PGM-free CLs, due to low mass activity comparing to PGM catalyst, the CLs are often 20 times thicker which leads to sever mass transport loss at high current density. Mass transport due to ionomer distribution, ionomer/catalyst interface, agglomerate heterogeneity can be tuned with the aid of colloid science, rheology, and fuel cell diagnostics.

APPENDIX
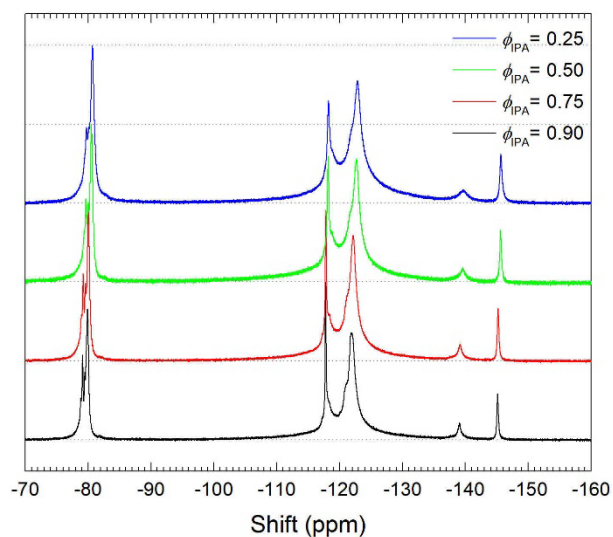
Figure A.1. ^{19}F NMR spectra of Nafion ionomer in water/IPA mixture of various IPA volume fractions.
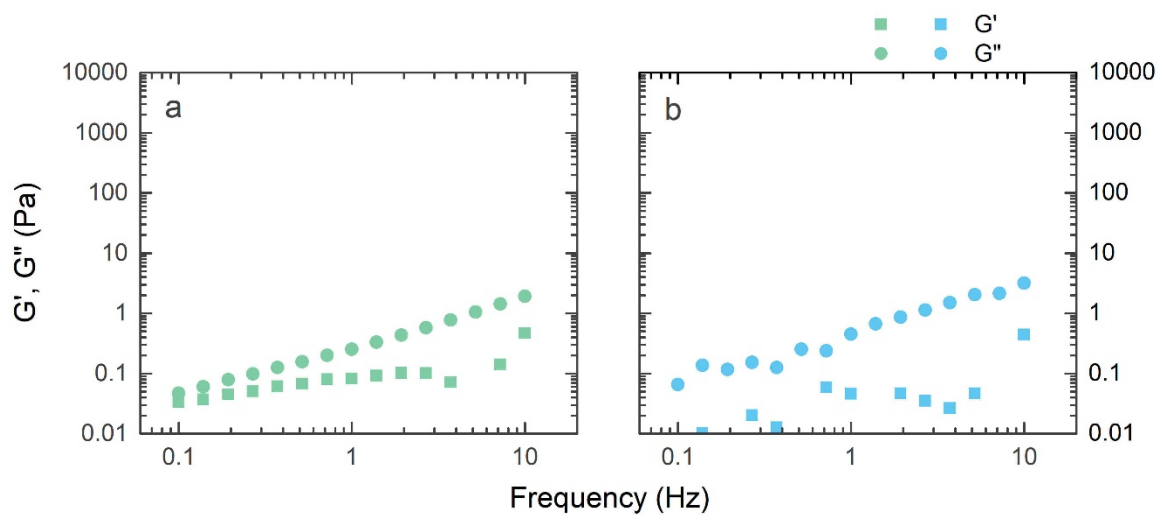
Figure A.2. Frequency-dependent linear viscoelastic properties of concentrated ionomer, in (a) water-rich and (b) IPA-rich liquid medium, respectively. Squares are for elastic modulus, G' and circle are for viscous modulus, G''. The ionomer concentrations in liquid phase remain the same as 61.5 mg/mL liquid.
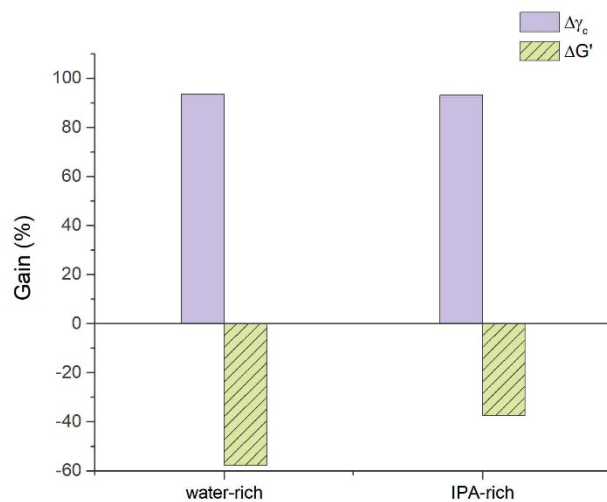
Figure A.3. Structural change due to prolonged exposure (>60 s) to high shear (1000 1/s) of the ionomer-PGM/C assemblages in both water-rich and IPA-rich environments.
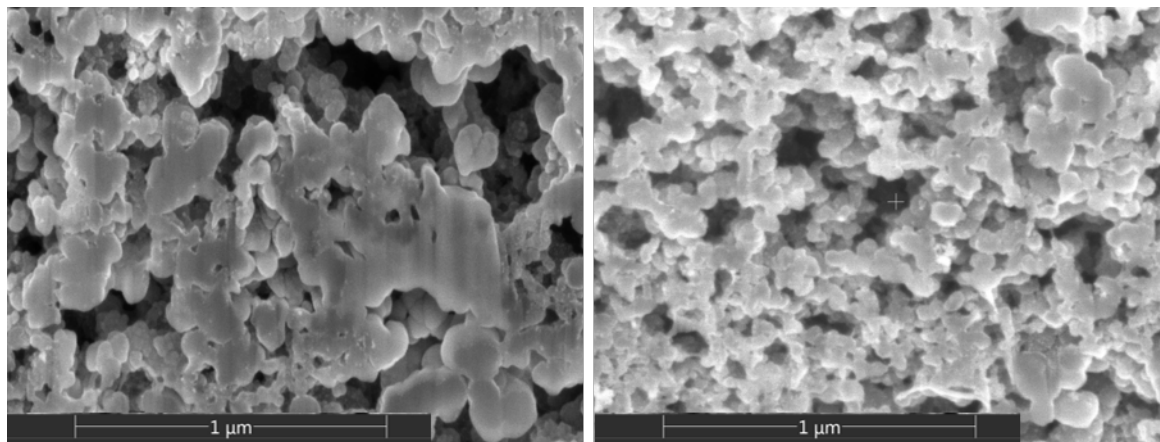
Figure A.4. Cross-section FIB-SEM images of water-rich (left) and IPA-rich (right) pristine catalyst layers.

Table A.1. Dynamic light scattering and electrophoretic light scattering data.

Sample	Z_{peak} (nm)	Z_{avg} (nm)	PDI	Electrophoresis Mobility ($\mu m \cdot cm/V \cdot s$)	Conductivity (mS/cm)
Water-rich					
i_25	86.01 ± 29.23	72.07	0.244	-0.4190 ± 0.02797	0.00126
C_25	233.4 ± 55.42	217.4	0.114	-0.6108 ± 0.01597	0.00211
i-C_25	335.8 ± 127.3	294.5	0.128	-1.224 ± 0.01990	0.00191
Pt/C_25	252.9 ± 50.70	236.7	0.127	-0.6849 ± 0.02441	0.00136
i-Pt/C_25	346.6 ± 120.8	305.4	0.174	-1.117 ± 0.04352	0.00233
IPA-rich					
i_25	166.3 ± 47.69	170.7	1	-0.1434 ± 0.01294	0.00058
C_25	264.9 ± 69.48	246.6	0.048	-0.2747 ± 0.003137	0.00297
i-C_25	368.4 ± 88.22	347.7	0.041	-0.3653 ± 0.01111	0.00169
Pt/C_25	272.0 ± 97.86	246.0	0.134	-0.2642 ± 0.006326	0.00249
i-Pt/C_25	236.4 ± 76.60	224.7	0.183	-0.2084 ± 0.01061	0.00332

REFERENCES

1. Administration, U. S. E. I., International Energy Outlook. 2016.
2. Stephens, I. E. L.; Rossmeisl, J.; Chorkendorff, I., Toward sustainable fuel cells. *Science* 2016, *354* (6318), 1378.
3. Administration, U. S. E. I., International Energy Outlook. 2018.
4. Dincer, I.; Rosen, M. A., Sustainability aspects of hydrogen and fuel cell systems. *Energy for Sustainable Development* 2011, *15* (2), 137-146.
5. Wang, Y.; Chen, K. S.; Mishler, J.; Cho, S. C.; Adroher, X. C., A review of polymer electrolyte membrane fuel cells: Technology, applications, and needs on fundamental research. *Applied Energy* 2011, *88* (4), 981-1007.
6. Cano, Z. P.; Banham, D.; Ye, S.; Hintennach, A.; Lu, J.; Fowler, M.; Chen, Z., Batteries and fuel cells for emerging electric vehicle markets. *Nature Energy* 2018, *3* (4), 279-289.
7. Papageorgopoulos, D. In *Fuel cell R&D overview*, DOE Hydrogen and Fuel Cells Program Annual Merit Review and Peer Evaluation Meeting, U.S. Department of Energy: 2019.
8. Banham, D.; Ye, S., Current Status and Future Development of Catalyst Materials and Catalyst Layers for Proton Exchange Membrane Fuel Cells: An Industrial Perspective. *ACS Energy Letters* 2017, *2* (3), 629-638.
9. Whiston, M. M.; Azevedo, I. L.; Litster, S.; Whitefoot, K. S.; Samaras, C.; Whitacre, J. F., Expert assessments of the cost and expected future performance of proton exchange membrane fuel cells for vehicles. *Proceedings of the National Academy of Sciences* 2019, *116* (11), 4899.
10. Banham, D.; Choi, J.-Y.; Kishimoto, T.; Ye, S., Integrating PGM-Free Catalysts into Catalyst Layers and Proton Exchange Membrane Fuel Cell Devices. *Advanced Materials* 2019, *0* (0), 1804846.
11. Borup, R. L.; Weber, A. Z. In *FC-PAD: Fuel Cell Performance and Durability Consortium*, DOE Hydrogen and Fuel Cells Program Annual Merit Review and Peer Evaluation Meeting, U.S. Department of Energy: 2019.
12. Wilson, M. S.; Gottesfeld, S., Thin-film catalyst layers for polymer electrolyte fuel cell electrodes. *Journal of Applied Electrochemistry* 1992, *22* (1), 1-7.
13. Wilson, M. S.; Gottesfeld, S., High Performance Catalyzed Membranes of Ultra-low Pt Loadings for Polymer Electrolyte Fuel Cells. *Journal of The Electrochemical Society* 1992, *139* (2), L28-L30.
14. Banham, D.; Kishimoto, T.; Zhou, Y.; Sato, T.; Bai, K.; Ozaki, J.-i.; Imashiro, Y.; Ye, S., Critical advancements in achieving high power and stable

nonprecious metal catalyst–based MEAs for real-world proton exchange membrane fuel cell applications. *Science Advances* 2018, *4* (3), eaar7180.

15. Mauger, S. A.; Neyerlin, K. C.; Yang-Neyerlin, A. C.; More, K. L.; Ulsh, M., Gravure Coating for Roll-to-Roll Manufacturing of Proton-Exchange-Membrane Fuel Cell Catalyst Layers. *Journal of The Electrochemical Society* 2018, *165* (11), F1012-F1018.

16. Zamel, N., The catalyst layer and its dimensionality – A look into its ingredients and how to characterize their effects. *Journal of Power Sources* 2016, *309*, 141-159.

17. Takahashi, S.; Mashio, T.; Horibe, N.; Akizuki, K.; Ohma, A., Analysis of the Microstructure Formation Process and Its Influence on the Performance of Polymer Electrolyte Fuel-Cell Catalyst Layers. *ChemElectroChem* 2015, *2* (10), 1560-1567.

18. Kumano, N.; Kudo, K.; Suda, A.; Akimoto, Y.; Ishii, M.; Nakamura, H., Controlling cracking formation in fuel cell catalyst layers. *Journal of Power Sources* 2019, *419*, 219-228.

19. Hong, S.; Hou, M.; Zhang, H.; Jiang, Y.; Shao, Z.; Yi, B., A high-performance PEM fuel cell with ultralow platinum electrode via electrospinning and underpotential deposition. *Electrochimica Acta* 2017, *245* (Generic), 403-409.

20. Slack, J. J.; Gumeci, C.; Dale, N.; Parrondo, J.; Macauley, N.; Mukundan, R.; Cullen, D.; Sneed, B.; More, K.; Pintauro, P. N., Nanofiber Fuel Cell MEAs with a PtCo/C Cathode. *Journal of the Electrochemical Society* 2019, *166* (7), F3209.

21. Jiang, S. F.; Yi, B. L.; Cao, L. S.; Song, W.; Zhao, Q.; Yu, H. M.; Shao, Z. G., Development of advanced catalytic layer based on vertically aligned conductive polymer arrays for thin-film fuel cell electrodes. *Journal of Power Sources* 2016, *329*, 347-354.

22. Sun, R.; Xia, Z.; Li, H.; Jing, F.; Wang, S., Ordered Nafion® ionomers decorated polypyrrole nanowires for advanced electrochemical applications. *Journal of Energy Chemistry* 2018, *27* (3), 854-858.

23. O'Hayre, R.; Prinz, F. B., The Air/Platinum/Nafion Triple-Phase Boundary: Characteristics, Scaling, and Implications for Fuel Cells. *Journal of The Electrochemical Society* 2004, *151* (5), A756-A762.

24. O'Hayre, R.; Barnett, D. M.; Prinz, F. B., The Triple Phase Boundary: A Mathematical Model and Experimental Investigations for Fuel Cells. *Journal of The Electrochemical Society* 2005, *152* (2), A439-A444.

25. Orfanidi, A.; Madkikar, P.; El-Sayed, H. A.; Harzer, G. S.; Kratky, T.; Gasteiger, H. A., The Key to High Performance Low Pt Loaded Electrodes. *Journal of the Electrochemical Society* 2017, *164* (4), F418-F426.

26. Harzer, G. S.; Schwammlein, J. N.; Damjanovic, A. M.; Ghosh, S.; Gasteiger, H. A., Cathode Loading Impact on Voltage Cycling Induced PEMFC Degradation: A Voltage Loss Analysis. *Journal of the Electrochemical Society* 2018, *165* (6), F3118-F3131.

27. Muzaffar, T.; Kadyk, T.; Eikerling, M., Tipping water balance and the Pt loading effect in polymer electrolyte fuel cells: a model-based analysis. *Sustainable Energy & Fuels* 2018, *2* (6), 1189-1196.

28. Freiberg, A. T. S.; Tucker, M. C.; Weber, A. Z., Polarization loss correction derived from hydrogen local-resistance measurement in low Pt-loaded polymer-electrolyte fuel cells. *Electrochemistry Communications* 2017, *79*, 14-17.

29. Cetinbas, F. C.; Ahluwalia, R. K., Agglomerates in Polymer Electrolyte Fuel Cell Electrodes: Part II. Transport Characterization. *Journal of the Electrochemical Society* 2018, *165* (13), F1059-F1066.

30. Yu, H.; Bonville, L.; Maric, R., Analysis of H_2/Air Polarization Curves: The Influence of Low Pt Loading and Fabrication Process. *Journal of The Electrochemical Society* 2018, *165* (5), F272-F284.

31. Sassin, M. B.; Garsany, Y.; Atkinson, R. W.; Hjelm, R. M. E.; Swider-Lyons, K. E., Understanding the interplay between cathode catalyst layer porosity and thickness on transport limitations en route to high-performance PEMFCs. *International Journal of Hydrogen Energy* 2019.

32. Malko, D.; Lopes, T.; Ticianelli, E. A.; Kucernak, A., A catalyst layer optimisation approach using electrochemical impedance spectroscopy for PEM fuel cells operated with pyrolysed transition metal-N-C catalysts. *Journal of Power Sources* 2016, *323*, 189-200.

33. Park, J. C.; Choi, C. H., Graphene-derived Fe/Co-N-C catalyst in direct methanol fuel cells: Effects of the methanol concentration and ionomer content on cell performance. *Journal of Power Sources* 2017, *358*, 76-84.

34. Huang, J.; Li, Z.; Zhang, J., Review of characterization and modeling of polymer electrolyte fuel cell catalyst layer: The blessing and curse of ionomer. *Frontiers in Energy* 2017, *11* (3), 334-364.

35. Takahashi, S.; Shimanuki, J.; Mashio, T.; Ohma, A.; Tohma, H.; Ishihara, A.; Ito, Y.; Nishino, Y.; Miyazawa, A., Observation of ionomer in catalyst ink of polymer electrolyte fuel cell using cryogenic transmission electron microscopy. *Electrochimica Acta* 2017, *224*, 178-185.

36. Normile, S. J.; Sabarirajan, D. C.; Calzada, O.; De Andrade, V.; Xiao, X.; Mandal, P.; Parkinson, D. Y.; Serov, A.; Atanassov, P.; Zenyuk, I. V., Direct observations of liquid water formation at nano- and micro-scale in platinum group metal-free electrodes by operando X-ray computed tomography. *Materials Today Energy* 2018, *9*, 187-197.

37. Inoue, G.; Kawase, M., Understanding formation mechanism of heterogeneous porous structure of catalyst layer in polymer electrolyte fuel cell. *International Journal of Hydrogen Energy* 2016, *41* (46), 21352-21365.

38. Karan, K., PEFC catalyst layer: Recent advances in materials, microstructural characterization, and modeling. *Current Opinion in Electrochemistry* 2017, *5* (1), 27-35.

39. Xu, F.; Zhang, H.; Ilavsky, J.; Stanciu, L.; Ho, D.; Justice, M. J.; Petrache, H. I.; Xie, J., Investigation of a Catalyst Ink Dispersion Using Both Ultra-Small-Angle X-ray Scattering and Cryogenic TEM. *Langmuir* 2010, *26* (24), 19199-19208.

40. Lousenberg, R. D., Molar mass distributions and viscosity behavior of perfluorinated sulfonic acid polyelectrolyte aqueous dispersions. *Journal of Polymer Science Part B: Polymer Physics* 2005, *43* (4), 421-428.

41. Strong, A.; Britton, B.; Edwards, D.; Peckham, T. J.; Lee, H.-F.; Huang, W. Y.; Holdcroft, S., Alcohol-Soluble, Sulfonated Poly(arylene ether)s: Investigation of Hydrocarbon Ionomers for Proton Exchange Membrane Fuel Cell Catalyst Layers. *Journal of The Electrochemical Society* 2015, *162* (6), F513-F518.

42. Ngo, T. T.; Yu, T. L.; Lin, H.-L., Influence of the composition of isopropyl alcohol/water mixture solvents in catalyst ink solutions on proton exchange membrane fuel cell performance. *Journal of Power Sources* 2013, *225*, 293-303.

43. Xie, Z.; Zhao, X.; Adachi, M.; Shi, Z.; Mashio, T.; Ohma, A.; Shinohara, K.; Holdcroft, S.; Navessin, T., Fuel cell cathode catalyst layers from "green" catalyst inks. *Energy & Environmental Science* 2008, *1* (1), 184-193.

44. Devaraj, V.; Lopez, L. F.; Beaman, J. J.; Prudhomme, S., Model-Based Control of a Continuous Coating Line for Proton Exchange Membrane Fuel Cell Electrode Assembly. *International Journal of Chemical Engineering (1687806X)* 2015, *2015*, 1-11.

45. Ulsh, M.; Porter, J. M.; Bittinat, D. C.; Bender, G., Defect Detection in Fuel Cell Gas Diffusion Electrodes Using Infrared Thermography. *Fuel Cells* 2016, *16* (2), 170-178.

46. Steenberg, T.; Hjuler, H. A.; Terkelsen, C.; Sánchez, M. T. R.; Cleemann, L. N.; Krebs, F. C., Roll-to-roll coated PBI membranes for high temperature PEM fuel cells. *Energy & Environmental Science* 2012, *5* (3), 6076-6080.

47. Glüsen, A.; Müller, M.; Stolten, D., Slot-Die Coating: A New Preparation Method for Direct Methanol Fuel Cells Catalyst Layers. *Journal of Fuel Cell.Science and Technology* 2013, *10* (4), 4.

48. Alink, R.; Schüßler, M.; Pospischil, M.; Erath, D.; Gerteisen, D., Analyzing the influence of high electrode potentials on intrinsic properties of catalyst

coated membranes using impedance spectroscopy. *Journal of Power Sources* 2016, *327*, 526-534.

49. Schonert, M.; Jakoby, K.; Schlumbohm, C.; Glüsen, A.; Mergel, J.; Stolten, D., Manufacture of Robust Catalyst Layers for the DMFC. *Fuel Cells* 2004, *4* (3), 175-179.

50. Su, H.; Jao, T.-C.; Barron, O.; Pollet, B. G.; Pasupathi, S., Low platinum loading for high temperature proton exchange membrane fuel cell developed by ultrasonic spray coating technique. *Journal of Power Sources* 2014, *267*, 155-159.

51. Yu, H.; Roller, J. M.; Mustain, W. E.; Maric, R., Influence of the ionomer/carbon ratio for low-Pt loading catalyst layer prepared by reactive spray deposition technology. *Journal of Power Sources* 2015, *283*, 84-94.

52. Borghetti, M.; Serpelloni, M.; Sardini, E.; Pandini, S., Mechanical behavior of strain sensors based on PEDOT:PSS and silver nanoparticles inks deposited on polymer substrate by inkjet printing. *Sensors and Actuators A: Physical* 2016, *243*, 71-80.

53. Şanlı, L. I.; Yarar, B.; Bayram, V.; Gürsel, S. A., Electrosprayed catalyst layers based on graphene–carbon black hybrids for the next-generation fuel cell electrodes. *Journal of Materials Science* 2017, *52* (4), 2091-2102.

54. Kusano, T.; Hiroi, T.; Amemiya, K.; Ando, M.; Takahashi, T.; Shibayama, M., Structural evolution of a catalyst ink for fuel cells during the drying process investigated by CV-SANS. *Polymer Journal* 2015, *47*, 546.

55. Hatzell, K. B.; Dixit, M. B.; Berlinger, S. A.; Weber, A. Z., Understanding inks for porous-electrode formation. *Journal of Materials Chemistry A* 2017, *5* (39), 20527-20533.

56. Holdcroft, S., Fuel Cell Catalyst Layers: A Polymer Science Perspective. *Chemistry of Materials* 2014, *26* (1), 381-393.

57. Zhang, H.; Wang, X.; Zhang, J.; Zhang, J., Conventional Catalyst Ink, Catalyst Layer and MEA Preparation. In *PEM Fuel Cell Electrocatalysts and Catalyst Layers: Fundamentals and Applications*, Zhang, J., Ed. Springer London: London, 2008; pp 889-916.

58. Lobato, J.; Rodrigo, M. A.; Linares, J. J.; Scott, K., Effect of the catalytic ink preparation method on the performance of high temperature polymer electrolyte membrane fuel cells. *Journal of Power Sources* 2006, *157* (1), 284-292.

59. Sung, K. A.; Jung, H.-Y.; Kim, W.-K.; Cho, K.-Y.; Park, J.-K., Influence of dispersion solvent for catalyst ink containing sulfonated poly(ether ether ketone) on cathode behaviour in a direct methanol fuel cell. *Journal of Power Sources* 2007, *169* (2), 271-275.

60. Xie, Z.; Zhao, X.; Adachi, M.; Shi, Z.; Mashio, T.; Ohma, A.; Shinohara, K.; Holdcroft, S.; Navessin, T., Fuel cell cathode catalyst layers from "green" catalyst inks. *Energy & Environmental Science* 2008, *1* (1), 184-193.

61. Chisaka, M.; Daiguji, H., Effect of Organic Solvents on Catalyst Layer Structure in Polymer Electrolyte Membrane Fuel Cells. *Journal of the Electrochemical Society* 2009, *156* (1), B22-B26.

62. Therdthianwong, A.; Ekdharmasuit, P.; Therdthianwong, S., Fabrication and Performance of Membrane Electrode Assembly Prepared by a Catalyst-Coated Membrane Method: Effect of Solvents Used in a Catalyst Ink Mixture. *Energy & Fuels* 2010, *24* (2), 1191-1196.

63. Bonifacio, R. N.; Armani Paschoal, J. O.; Linardi, M.; Cuenca, R., Catalyst layer optimization by surface tension control during ink formulation of membrane electrode assemblies in proton exchange membrane fuel cell. *Journal of Power Sources* 2011, *196* (10), 4680-4685.

64. Huang, D.-C.; Yu, P.-J.; Liu, F.-J.; Huang, S.-L.; Hsueh, K.-L.; Chen, Y.-C.; Wu, C.-H.; Chang, W.-C.; Tsau, F.-H., Effect of Dispersion Solvent in Catalyst Ink on Proton Exchange Membrane Fuel Cell Performance. *International Journal of Electrochemical Science* 2011, *6* (7), 2551-2565.

65. Jung, C.-Y.; Kim, W.-J.; Yi, S.-C., Optimization of catalyst ink composition for the preparation of a membrane electrode assembly in a proton exchange membrane fuel cell using the decal transfer. *International Journal of Hydrogen Energy* 2012, *37* (23), 18446-18454.

66. Welch, C.; Labouriau, A.; Hjelm, R.; Orler, B.; Johnston, C.; Kim, Y. S., Nafion in Dilute Solvent Systems: Dispersion or Solution? *ACS Macro Letters* 2012, *1* (12), 1403-1407.

67. Kim, Y. S.; Welch, C. F.; Hjelm, R. P.; Mack, N. H.; Labouriau, A.; Orler, E. B., Origin of Toughness in Dispersion-Cast Nafion Membranes. *Macromolecules* 2015, *48* (7), 2161-2172.

68. Ma, S.; Chen, Q.; Jøgensen, F. H.; Stein, P. C.; Skou, E. M., 19F NMR studies of Nafion™ ionomer adsorption on PEMFC catalysts and supporting carbons. *Solid State Ionics* 2007, *178* (29), 1568-1575.

69. Andersen, S. M., Nano carbon supported platinum catalyst interaction behavior with perfluorosulfonic acid ionomer and their interface structures. *Applied Catalysis B: Environmental* 2016, *181*, 146-155.

70. Yang, F.; Xin, L.; Uzunoglu, A.; Qiu, Y.; Stanciu, L.; Ilavsky, J.; Li, W.; Xie, J., Investigation of the Interaction between Nafion Ionomer and Surface Functionalized Carbon Black Using Both Ultrasmall Angle X-ray Scattering and Cryo-TEM. *ACS Applied Materials & Interfaces* 2017, *9* (7), 6530-6538.

71. Mashio, T.; Ohma, A.; Tokumasu, T., Molecular Dynamics Study of Ionomer Adsorption at a Carbon Surface in Catalyst Ink. *Electrochimica Acta* 2016, *202* (Generic), 14-23.

72. Khandavalli, S.; Park, J. H.; Kariuki, N. N.; Myers, D. J.; Stickel, J. J.; Hurst, K.; Neyerlin, K. C.; Ulsh, M.; Mauger, S. A., Rheological Investigation on the Microstructure of Fuel Cell Catalyst Inks. *ACS Applied Materials & Interfaces* 2018, *10* (50), 43610-43622.

73. Malek, K.; Eikerling, M.; Wang, Q.; Navessin, T.; Liu, Z., Self-Organization in Catalyst Layers of Polymer Electrolyte Fuel Cells. *The Journal of Physical Chemistry C* 2007, *111* (36), 13627-13634.

74. Shibayama, M.; Matsunaga, T.; Kusano, T.; Amemiya, K.; Kobayashi, N.; Yoshida, T., SANS studies on catalyst ink of fuel cell. *Journal of Applied Polymer Science* 2014, *131* (3).

75. Kusano, T.; Hiroi, T.; Amemiya, K.; Ando, M.; Takahashi, T.; Shibayama, M., Structural evolution of a catalyst ink for fuel cells during the drying process investigated by CV-SANS. *Polymer Journal* 2015, *47* (8), 546-555.

76. Suzuki, T.; Tanaka, H.; Hayase, M.; Tsushima, S.; Hirai, S., Investigation of porous structure formation of catalyst layers for proton exchange membrane fuel cells and their effect on cell performance. *International Journal of Hydrogen Energy* 2016, *41* (44), 20326-20335.

77. Luo, H.; Cardinal, C. M.; Scriven, L. E.; Francis, L. F., Ceramic Nanoparticle/Monodisperse Latex Coatings. *Langmuir* 2008, *24* (10), 5552-5561.

78. Malek, K.; Mashio, T.; Eikerling, M., Microstructure of Catalyst Layers in PEM Fuel Cells Redefined: A Computational Approach. *Electrocatalysis* 2011, *2* (2), 141.

79. So, M.; Park, K.; Ohnishi, T.; Ono, M.; Tsuge, Y.; Inoue, G., A discrete particle packing model for the formation of a catalyst layer in polymer electrolyte fuel cells. *International Journal of Hydrogen Energy* 2019.

80. Hosokawa, M.; Nogi, K.; Naito, M.; Yokoyama, T., *Nanoparticle Technology Handbook*. Elsevier: Saint Louis, THE NETHERLANDS 2007.

81. Chhabra, R. P.; Richardson, J. F., Chapter 4 - Flow of Multi-phase Mixtures in Pipes. In *Non-Newtonian Flow and Applied Rheology (Second Edition)*, Chhabra, R. P.; Richardson, J. F., Eds. Butterworth-Heinemann: Oxford, 2008; pp 206-248.

82. Wang, M.; Park, J. H.; Kabir, S.; Neyerlin, K. C.; Kariuki, N. N.; Lv, H.; Stamenkovic, V. R.; Myers, D. J.; Ulsh, M.; Mauger, S. A., Impact of Catalyst Ink Dispersing Methodology on Fuel Cell Performance Using in-Situ X-ray Scattering. *ACS Applied Energy Materials* 2019, *2* (9), 6417-6427.

83. Talukdar, K.; Ripan, M. A.; Jahnke, T.; Gazdzicki, P.; Morawietz, T.; Friedrich, K. A., Experimental and numerical study on catalyst layer of polymer electrolyte membrane fuel cell prepared with diverse drying methods. *Journal of Power Sources* 2020, *461*, 228169.

84. Brinker, C. J.; Scherer, G. W., *Sol-Gel Science : The Physics and Chemistry of Sol-Gel Processing*. Elsevier Science & Technology: San Diego, UNITED STATES, 1990.

85. Hench, L. L.; West, J. K., The sol-gel process. *Chemical Reviews* 1990, *90* (1), 33-72.

86. Mewis, J.; Wagner, N. J., *Colloidal Suspension Rheology*. Cambridge University Press: 2012.

87. Zaccarelli, E., Colloidal gels: equilibrium and non-equilibrium routes. *Journal of Physics: Condensed Matter* 2007, *19* (32), 323101.

88. Richards, J. J.; Hipp, J. B.; Riley, J. K.; Wagner, N. J.; Butler, P. D., Clustering and Percolation in Suspensions of Carbon Black. *Langmuir* 2017, *33* (43), 12260-12266.

89. Jiang, J.-S.; Guo, R.-H.; Chiu, Y.-S.; Hua, C.-C., Percolation behaviors of model carbon black pastes. *Soft Matter* 2018, *14* (48), 9786-9797.

90. Hipp, J. B.; Richards, J. J.; Wagner, N. J., Structure-property relationships of sheared carbon black suspensions determined by simultaneous rheological and neutron scattering measurements. *Journal of Rheology* 2019, *63* (3), 423-436.

91. Kusoglu, A.; Weber, A. Z., New Insights into Perfluorinated Sulfonic-Acid Ionomers. *Chemical Reviews* 2017, *117* (3), 987-1104.

92. Szajdzinska-Pietek, E.; Wolszczak, M.; Plonka, A.; Schlick, S., Structure and Dynamics of Micellar Aggregates in Aqueous Nafion Solutions Reported by Electron Spin Resonance and Fluorescence Probes. *Macromolecules* 1999, *32* (22), 7454-7460.

93. Dudenas, P. J.; Kusoglu, A., Evolution of Ionomer Morphology from Dispersion to Film: An in Situ X-ray Study. *Macromolecules* 2019.

94. Kronberg, B.; Holmberg, K.; Lindman, B. r., *Surface chemistry of surfactants and polymers*. Wiley: Chichester, West Sussex, 2014.

95. Bass, M.; Berman, A.; Singh, A.; Konovalov, O.; Freger, V., Surface-Induced Micelle Orientation in Nafion Films. *Macromolecules* 2011, *44* (8), 2893-2899.

96. Bredol, M.; Szydło, A.; Radev, I.; Philippi, W.; Bartholomäus, R.; Peinecke, V.; Heinzel, A., How the colloid chemistry of precursor electrocatalyst dispersions is related to the polymer electrolyte membrane fuel cell performance. *Journal of Power Sources* 2018, *402*, 15-23.

97. Ott, S.; Orfanidi, A.; Schmies, H.; Anke, B.; Nong, H. N.; Hübner, J.; Gernert, U.; Gliech, M.; Lerch, M.; Strasser, P., Ionomer distribution control in porous

carbon-supported catalyst layers for high-power and low Pt-loaded proton exchange membrane fuel cells. *Nature Materials* 2019.

98. Murthi, V. In *Durable MEAs for heavy-duty fuel cell electric trucks*, DOE Hydrogen and Fuel Cells Program Annual Merit Review and Peer Evaluation Meeting, 2020.

99. Darling, R. In *High performance PEFC electrode structures*, DOE Hydrogen and Fuel Cells Program Annual Merit Review and Peer Evaluation Meeting, 2020.

100. Kongkanand, A.; Mathias, M. F., The Priority and Challenge of High-Power Performance of Low-Platinum Proton-Exchange Membrane Fuel Cells. *The Journal of Physical Chemistry Letters* 2016, *7* (7), 1127-1137.

101. Cetinbas, F. C.; Wang, X. H.; Ahluwalia, R. K.; Kariuki, N. N.; Winarski, R. P.; Yang, Z. W.; Sharman, J.; Myers, D. J., Microstructural Analysis and Transport Resistances of Low-Platinum-Loaded PEFC Electrodes. *Journal of the Electrochemical Society* 2017, *164* (14), F1596-F1607.

102. Mu, Y.-T.; Weber, A. Z.; Gu, Z.-L.; Schuler, T.; Tao, W.-Q., Mesoscopic analyses of the impact of morphology and operating conditions on the transport resistances in a proton-exchange-membrane fuel-cell catalyst layer. *Sustainable Energy & Fuels* 2020, *4* (7), 3623-3639.

103. Schuler, T.; Chowdhury, A.; Freiberg, A. T.; Sneed, B.; Spingler, F. B.; Tucker, M. C.; More, K. L.; Radke, C. J.; Weber, A. Z., Fuel-Cell Catalyst-Layer Resistance via Hydrogen Limiting-Current Measurements. *Journal of The Electrochemical Society* 2019, *166* (7), F3020-F3031.

104. Geier, O.; Vasenkov, S.; Kärger, J., Pulsed field gradient nuclear magnetic resonance study of long–range diffusion in beds of NaX zeolite: Evidence for different apparent tortuosity factors in the Knudsen and bulk regimes. *The Journal of Chemical Physics* 2002, *117* (5), 1935-1938.

105. Malek, K.; Coppens, M.-O., Knudsen self- and Fickian diffusion in rough nanoporous media. *The Journal of Chemical Physics* 2003, *119* (5), 2801-2811.

106. Jinnouchi, R.; Kudo, K.; Kitano, N.; Morimoto, Y., Molecular Dynamics Simulations on O2 Permeation through Nafion Ionomer on Platinum Surface. *Electrochimica Acta* 2016, *188*, 767-776.

107. Ramaswamy, N.; Kumaraguru, S.; Koestner, R.; Fuller, T.; Gu, W.; Kariuki, N.; Myers, D.; Dudenas, P. J.; Kusoglu, A., Editors' Choice—Ionomer Side Chain Length and Equivalent Weight Impact on High Current Density Transport Resistances in PEMFC Cathodes. *Journal of The Electrochemical Society* 2021, *168* (2), 024518.

108. Yarlagadda, V.; Carpenter, M. K.; Moylan, T. E.; Kukreja, R. S.; Koestner, R.; Gu, W.; Thompson, L.; Kongkanand, A., Boosting Fuel Cell Performance with Accessible Carbon Mesopores. *ACS Energy Letters* 2018, *3* (3), 618-621.

109. Katzenberg, A.; Chowdhury, A.; Fang, M.; Weber, A. Z.; Okamoto, Y.; Kusoglu, A.; Modestino, M. A., Highly Permeable Perfluorinated Sulfonic Acid Ionomers for Improved Electrochemical Devices: Insights into Structure–Property Relationships. *Journal of the American Chemical Society* 2020, *142* (8), 3742-3752.

110. Novitski, D.; Holdcroft, S., Determination of O2 Mass Transport at the Pt | PFSA Ionomer Interface under Reduced Relative Humidity. *ACS Applied Materials & Interfaces* 2015, *7* (49), 27314-27323.

111. Conde, J. J.; Folgado, M. A.; Ferreira-Aparicio, P.; Chaparro, A. M.; Chowdhury, A.; Kusoglu, A.; Cullen, D.; Weber, A. Z., Mass-transport properties of electrosprayed Pt/C catalyst layers for polymer-electrolyte fuel cells. *Journal of Power Sources* 2019, *427*, 250-259.

112. Lopez-Haro, M.; Guétaz, L.; Printemps, T.; Morin, A.; Escribano, S.; Jouneau, P. H.; Bayle-Guillemaud, P.; Chandezon, F.; Gebel, G., Three-dimensional analysis of Nafion layers in fuel cell electrodes. *Nature Communications* 2014, *5*, 5229.

113. Kushner, D. I.; Kusoglu, A.; Podraza, N. J.; Hickner, M. A., Substrate-Dependent Molecular and Nanostructural Orientation of Nafion Thin Films. *Advanced Functional Materials* 2019, *29* (37), 1902699.

114. Morawietz, T.; Handl, M.; Oldani, C.; Friedrich, K. A.; Hiesgen, R., Quantitative in Situ Analysis of Ionomer Structure in Fuel Cell Catalytic Layers. *ACS Applied Materials & Interfaces* 2016, *8* (40), 27044-27054.

115. Komini Babu, S.; Chung, H. T.; Zelenay, P.; Litster, S., Resolving Electrode Morphology's Impact on Platinum Group Metal-Free Cathode Performance Using Nano-CT of 3D Hierarchical Pore and Ionomer Distribution. *ACS Applied Materials & Interfaces* 2016, *8* (48), 32764-32777.

116. Inoue, G.; Yokoyama, K.; Ooyama, J.; Terao, T.; Tokunaga, T.; Kubo, N.; Kawase, M., Theoretical examination of effective oxygen diffusion coefficient and electrical conductivity of polymer electrolyte fuel cell porous components. *Journal of Power Sources* 2016, *327*, 610-621.

117. Berne, B. J.; Pecora, R., *Dynamic light scattering: with applications to chemistry, biology, and physics*. Courier Corporation: 2000.

118. Larson, R. G., *Structure and Rheology of Complex Fluids*. Oxford University Press: 1999.

119. Mojica, F.; Rahman, M. A.; Sarker, M.; Hussey, D. S.; Jacobson, D. L.; LaManna, J. M.; Chuang, P.-Y. A., Study of converging-diverging channel induced convective mass transport in a proton exchange membrane fuel cell. *Energy Conversion and Management* 2021, *237*, 114095.

120. Trasatti, S.; Petrii, O. A., Real surface area measurements in electrochemistry. *Pure and Applied Chemistry* 1991, *63* (5), 711-734.

121. Baker, D. R.; Caulk, D. A.; Neyerlin, K. C.; Murphy, M. W., Measurement of Oxygen Transport Resistance in PEM Fuel Cells by Limiting Current Methods. *Journal of The Electrochemical Society* 2009, *156* (9), B991.

122. Hansen, C. M., *Hansen solubility parameters: a user's handbook.* 2nd ed.; CRC press: 2007.

123. Lee, S.-J.; Yu, T. L.; Lin, H.-L.; Liu, W.-H.; Lai, C.-L., Solution properties of nafion in methanol/water mixture solvent. *Polymer* 2004, *45* (8), 2853-2862.

124. Mima, T.; Kinjo, T.; Yamakawa, S.; Asahi, R., Study of the conformation of polyelectrolyte aggregates using coarse-grained molecular dynamics simulations. *Soft Matter* 2017, *13* (35), 5991-5999.

125. Su, W.-F., Polymer Size and Polymer Solutions. In *Principles of Polymer Design and Synthesis*, Su, W.-F., Ed. Springer Berlin Heidelberg: Berlin, Heidelberg, 2013; pp 9-26.

126. Kim, T.-H.; Yi, J.-Y.; Jung, C.-Y.; Jeong, E.; Yi, S.-C., Solvent effect on the Nafion agglomerate morphology in the catalyst layer of the proton exchange membrane fuel cells. *International Journal of Hydrogen Energy* 2017, *42* (1), 478-485.

127. Berlinger, S. A.; McCloskey, B. D.; Weber, A. Z., Inherent Acidity of Perfluorosulfonic Acid Ionomer Dispersions and Implications for Ink Aggregation. *The Journal of Physical Chemistry B* 2018, *122* (31), 7790-7796.

128. Ghelichi, M.; Malek, K.; Eikerling, M. H., Ionomer Self-Assembly in Dilute Solution Studied by Coarse-Grained Molecular Dynamics. *Macromolecules* 2016, *49* (4), 1479-1489.

129. Pecora, R., *Dynamic light scattering : applications of photon correlation spectroscopy.* Plenum Press: New York, 1985.

130. Fundamental Concepts. In *Light Scattering from Polymer Solutions and Nanoparticle Dispersions*, Schärtl, W., Ed. Springer Berlin Heidelberg: Berlin, Heidelberg, 2007; pp 1-24.

131. Pecora, R., Dynamic Light Scattering Measurement of Nanometer Particles in Liquids. *Journal of Nanoparticle Research* 2000, *2* (2), 123-131.

132. Mashio, T.; Malek, K.; Eikerling, M.; Ohma, A.; Kanesaka, H.; Shinohara, K., Molecular Dynamics Study of Ionomer and Water Adsorption at Carbon Support Materials. *The Journal of Physical Chemistry C* 2010, *114* (32), 13739-13745.

133. Hogg, R., Bridging Flocculation by Polymers. *KONA Powder and Particle Journal* 2013, *30*, 3-14.

134. Zeng, J.; Jean, D.-i.; Ji, C.; Zou, S., In Situ Surface-Enhanced Raman Spectroscopic Studies of Nafion Adsorption on Au and Pt Electrodes. *Langmuir* 2012, *28* (1), 957-964.

135. Tassieri, M.; Laurati, M.; Curtis, D. J.; Auhl, D. W.; Coppola, S.; Scalfati, A.; Hawkins, K.; Williams, P. R.; Cooper, J. M., i-Rheo: Measuring the materials' linear viscoelastic properties "in a step"! *Journal of Rheology* 2016, *60* (4), 649-660.

136. Nguyen, H. T.; Graham, A. L.; Koenig, P. H.; Gelb, L. D., Computer simulations of colloidal gels: how hindered particle rotation affects structure and rheology. *Soft Matter* 2020, *16* (1), 256-269.

137. Nguyen, Q. D.; Boger, D. V., Measuring the Flow Properties of Yield Stress Fluids. *Annual Review of Fluid Mechanics* 1992, *24* (1), 47-88.

138. Kistler, S. F.; Schweizer, P. M., *Liquid film coating : scientific principles and their technological implications*. Chapman & Hall: London ;, 1997.

139. Mewis, J.; Wagner, N. J., Thixotropy. *Advances in Colloid and Interface Science* 2009, *147-148*, 214-227.

140. Berlinger, S. A.; Dudenas, P. J.; Bird, A.; Chen, X.; Freychet, G.; McCloskey, B. D.; Kusoglu, A.; Weber, A. Z., Impact of Dispersion Solvent on Ionomer Thin Films and Membranes. *ACS Applied Polymer Materials* 2020, *2* (12), 5824-5834.

141. Shi, S.; Liu, Z.; Lin, Q.; Chen, X.; Kusoglu, A., Role of ionic interactions in the deformation and fracture behavior of perfluorosulfonic-acid membranes. *Soft Matter* 2020, *16* (6), 1653-1667.

142. Dixit, M. B.; Harkey, B. A.; Shen, F.; Hatzell, K. B., Catalyst Layer Ink Interactions That Affect Coatability. *Journal of the Electrochemical Society* 2018, *165* (5), F271.

143. Pietsch, W., *Agglomeration processes : phenomena, technologies, equipment*. Wiley-VCH: Weinheim, 2002.

144. Schmelzer, J.; Röpke, G.; Mahnke, R., *Aggregation phenomena in complex systems*. Wiley-VCH: Weinheim ;, 1999.

145. Zhao, K.; Mason, T. G., Assembly of colloidal particles in solution. *Reports on Progress in Physics* 2018, *81* (12), 126601.

146. Pramounmat, N.; Loney, C. N.; Kim, C.; Wiles, L.; Ayers, K. E.; Kusoglu, A.; Renner, J. N., Controlling the Distribution of Perfluorinated Sulfonic Acid Ionomer with Elastin-like Polypeptide. *ACS Applied Materials & Interfaces* 2019, *11* (46), 43649-43658.

147. Orfanidi, A.; Rheinländer, P. J.; Schulte, N.; Gasteiger, H. A., Ink Solvent Dependence of the Ionomer Distribution in the Catalyst Layer of a PEMFC. *Journal of The Electrochemical Society* 2018, *165* (14), F1254-F1263.

148. Cetinbas, F. C.; Ahluwalia, R. K.; Kariuki, N. N.; Myers, D. J., Agglomerates in Polymer Electrolyte Fuel Cell Electrodes: Part I. Structural Characterization. *Journal of the Electrochemical Society* 2018, *165* (13), F1051-F1058.

149. Inoue, G.; Ohnishi, T.; So, M.; Park, K.; Ono, M.; Tsuge, Y., Simulation of carbon black aggregate and evaluation of ionomer structure on carbon in catalyst layer of polymer electrolyte fuel cell. *Journal of Power Sources* 2019, *439*, 227060.

150. Mu, Y.-T.; Weber, A. Z.; Gu, Z.-L.; Tao, W.-Q., Mesoscopic modeling of transport resistances in a polymer-electrolyte fuel-cell catalyst layer: Analysis of hydrogen limiting currents. *Applied Energy* 2019, *255*, 113895.

151. Xie, J.; Xu, F.; Wood, D. L.; More, K. L.; Zawodzinski, T. A.; Smith, W. H., Influence of ionomer content on the structure and performance of PEFC membrane electrode assemblies. *Electrochimica Acta* 2010, *55* (24), 7404-7412.

152. Johnson, L. C.; Zia, R. N.; Moghimi, E.; Petekidis, G., Influence of structure on the linear response rheology of colloidal gels. *Journal of Rheology* 2019, *63* (4), 583-608.

153. Lazzari, S.; Nicoud, L.; Jaquet, B.; Lattuada, M.; Morbidelli, M., Fractal-like structures in colloid science. *Advances in Colloid and Interface Science* 2016, *235*, 1-13.

154. Conchuir, B. O.; Harshe, Y. M.; Lattuada, M.; Zaccone, A., Analytical Model of Fractal Aggregate Stability and Restructuring in Shear Flows. *Industrial & Engineering Chemistry Research* 2014, *53* (22), 9109-9119.

155. Liu, Y.; Murphy, M. W.; Baker, D. R.; Gu, W.; Ji, C.; Jorne, J.; Gasteiger, H. A., Proton Conduction and Oxygen Reduction Kinetics in PEM Fuel Cell Cathodes: Effects of Ionomer-to-Carbon Ratio and Relative Humidity. *Journal of The Electrochemical Society* 2009, *156* (8), B970.

156. Cetinbas, F. C.; Ahluwalia, R. K.; Kariuki, N. N.; De Andrade, V.; Myers, D. J., Effects of Porous Carbon Morphology, Agglomerate Structure and Relative Humidity on Local Oxygen Transport Resistance. *Journal of The Electrochemical Society* 2020, *167* (1).

157. Shimoaka, T.; Wakai, C.; Sakabe, T.; Yamazaki, S.; Hasegawa, T., Hydration structure of strongly bound water on the sulfonic acid group in a Nafion membrane studied by infrared spectroscopy and quantum chemical calculation. *Physical Chemistry Chemical Physics* 2015, *17* (14), 8843-8849.

158. Harzer, G. S.; Orfanidi, A.; El-Sayed, H.; Madkikar, P.; Gasteiger, H. A., Tailoring Catalyst Morphology towards High Performance for Low Pt Loaded PEMFC Cathodes. *Journal of the Electrochemical Society* 2018, *165* (10), F770-F779.